Hindawi
International Journal of Aerospace Engineering
Volume 2023, Article ID 8445145, 24 pages
https://doi.org/10.1155/2023/8445145

Research Article

Parameter Analysis of Active Flap Control for Rotor Aerodynamic Control and Design

Runze Xia, Zhiyuan Hu, Yongjie Shi, and Guohua Xu

National Key Laboratory of Helicopter Aeromechanics, Nanjing University of Aeronautics and Astronautics, Nanjing 210016, China

Correspondence should be addressed to Zhiyuan Hu; huzhiyuan@nuaa.edu.cn

Received 8 December 2022; Revised 9 February 2023; Accepted 9 June 2023; Published 29 June 2023

Academic Editor: Alex Zanotti

Active rotor control of helicopters is the future development direction, and active flap control (AFC) is one of the most promising technologies. However, the numerical simulation of an AFC rotor is challenging. It is necessary to consider the fidelity of the local flow details while dealing with complex shapes and motions. Therefore, few simulations of the flow field and analyses of the influencing parameters have been conducted. In particular, there is a lack of aerodynamic design criteria and recommendations for the AFC rotor. Thus, a new overset assembly algorithm, an arbitrary multilevel moving grid transformation algorithm, and a solver for the unsteady Reynolds-averaged Navier-Stokes equations (URANS) are proposed to establish a suitable numerical method for AFC rotor simulation. The aerodynamic characteristics of the rotor and key influencing factors are systematically analyzed under different flow conditions and design and control parameters, and suggestions for the design of the AFC rotor are provided. The results show that the AFC significantly changes the load distribution of the rotor. The thrust loss of the rotor is approximately 1%, but the offset angle compensates for the loss. The control parameters show relatively consistent trends under different working conditions. The phase is the key control parameter, and the effect on the load is more pronounced when the control frequency is an integral multiple of the rotor's natural load frequency. Increasing the chord length, span length, and deflection amplitude can also enhance the active control performance.

1. Introduction

Improving the rotor's performance and reducing aerodynamic noise and vibration are critical aspects of helicopter design. Active flap control (AFC) [1–3] has become a hot spot in helicopter rotor design in recent years due to its ability to reduce vibration and noise. The key feature of the AFC rotor is that the blade is equipped with a trailing edge flap (TEF), which deflects up and down relative to the main blade, as shown in Figure 1 [4–6]. The geometry of the blade can be dynamically changed by rotating the TEF.

AFC can control rotor vibration; for example, a BK117 helicopter equipped with AFC achieved substantial vibration reduction [7]. AFC can also be used for noise control. Chia et al. observed noise reduction of up to 6 dB [8]. In addition, it can also be used to improve the rotor performance. For example, Ravichandran et al. improved the hovering efficiency of a helicopter under a heavy load by deflecting the TEF downward [9]. AFC has also been applied to improve wind turbines' energy generation capacity and the power generation ability of wind tunnels [10, 11]. In the helicopter industry, the FRIENDCOPTER project [12] of Eurocopter and Airbus and the smart material-actuated rotor technology (SMART) [3, 13] by DARPA, NASA, and Boeing have fully verified the vibration reduction, noise reduction, power control, and performance of the AFC rotor and demonstrated the application prospect of this new active control technology.

Research on AFC rotors has primarily focused on the design and driving mechanism and the analysis of vibration

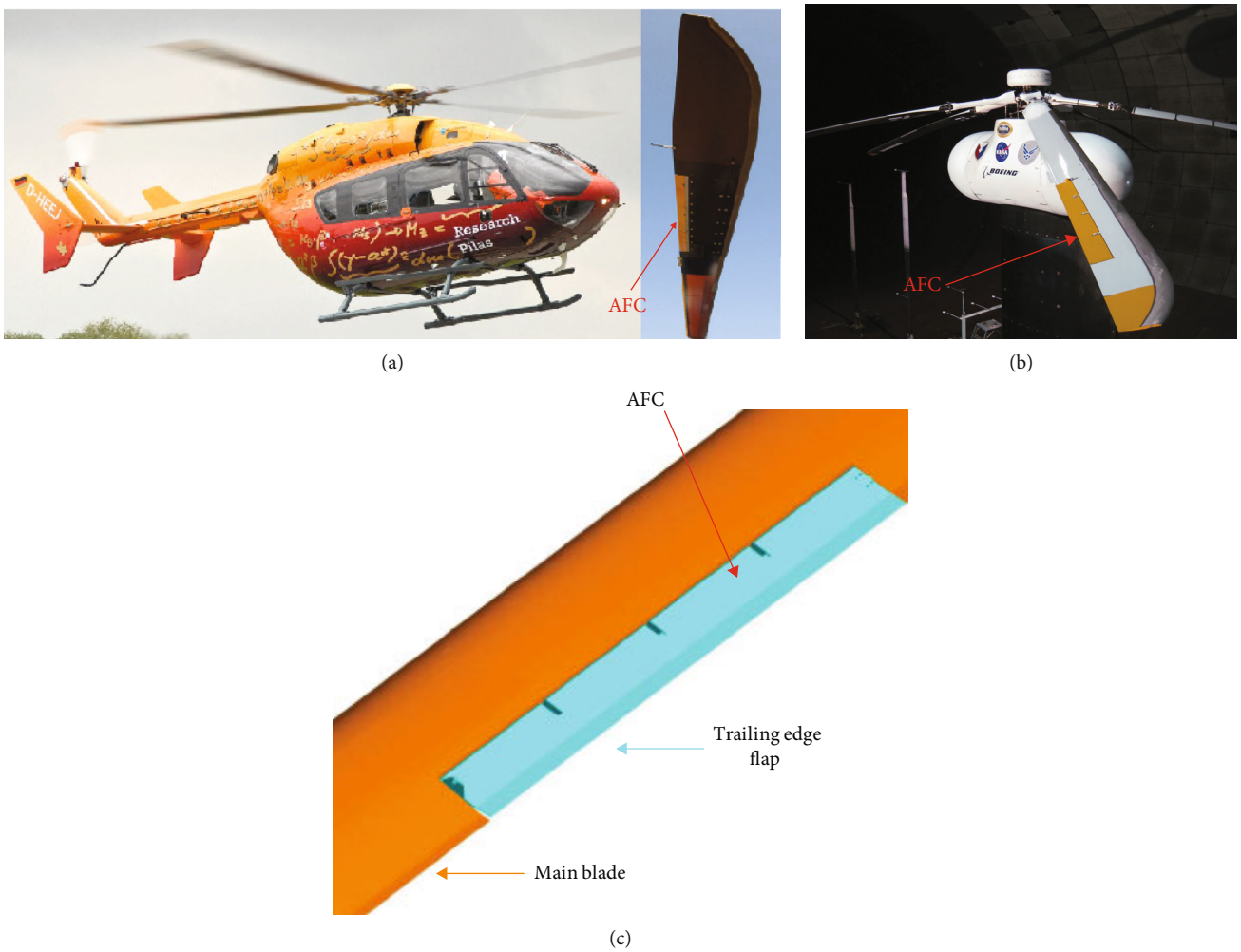

Figure 1: Active flap control rotor and its blades: (a) EC145 with AFC [4]; (b) Boeing-SMART rotor with AFC [5]; (c) MD900 blade with AFC [6].

reduction, noise reduction, or performance improvement. Many structural designs have been developed to manufacture rotors and achieve controllable deflection. AFC is powered by a piezoelectric actuator, electrohydraulic system [12], or other methods. Improved designs include the induced-shear piezoelectric actuator [14] and pneumatic artificial muscles based on bionic structures [15]. New controllers have been proposed, such as the adaptive and discrete-time model predictive controller. Most simulation studies have used computational fluid dynamics (CFD) calculations using a deformation mesh [16], overset grid [17, 18], or the newly developed viscous vortex particle method [19]. However, these simulation strategies must be meticulously designed and handled carefully.

Regarding AFC aerodynamics and performance research, the focus of this paper, Hassan et al. [20] tested and analyzed the HH-06 airfoil equipped with a TEF, considered the influence of the overhanging length on hinge moment, and provided guidance for the design of AFC airfoils. Xing et al. [21] studied the effect of a TEF on the dynamic stall vortex and unsteady aerodynamic force of a pitching airfoil. They observed a decrease in the maximum drag and pitching moment coefficient in the simulation and found that increasing the chord length was an effective control method. By optimizing the nonharmonic control law, Kody et al. achieved a power reduction of 9.5% at a large advance ratio [22] and improved the performance and vibration simultaneously by optimizing the control of a dual-segment TEF [23]. In addition, Jose and Baeder [18], the author's team [24], and Jain et al. [25] also discussed the aerodynamic performance loss caused by leakage flow in the gaps of the airfoil and rotor.

Many studies focused on the blade design of the AFC rotor and the characteristics of airfoils (including dynamic airfoils) with TEFs, but few conducted detailed analyses and comparisons of this rotor with different designs and control parameters. Multiple experiments have been conducted on existing AFC designs, such as SMART, including vibration control, noise control, and power control. However, these experiments used scaled rotors with specific shapes and did not consider different TEF sizes and installation positions. Thus, they cannot be used to improve the size, control performance, and design of AFC rotors. The

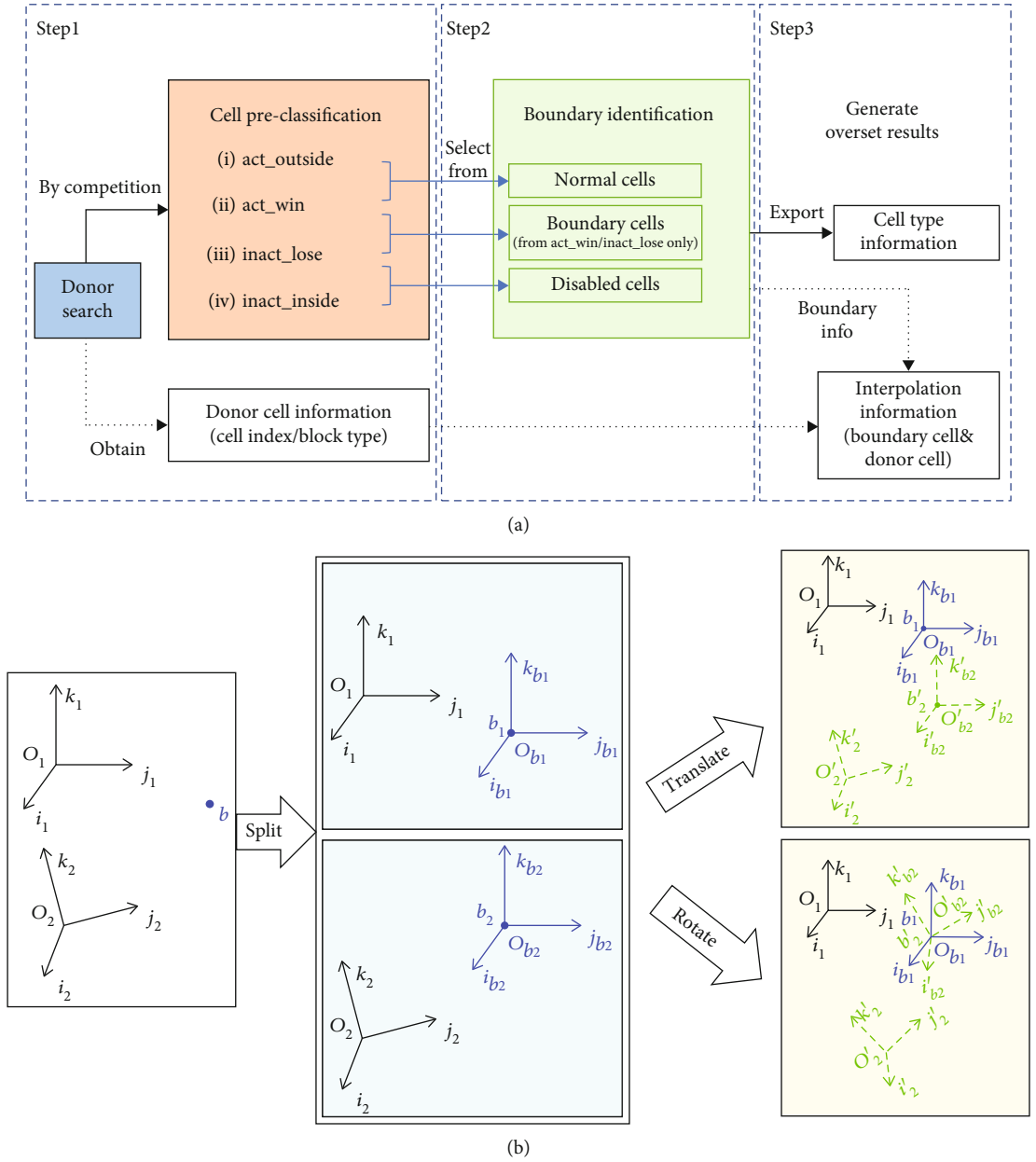

Figure 2: The overset assembly method of the motion grid: (a) steps of the ROAT method; (b) motion description based on multilevel coordinate system transformation.

main difficulties are as follows: (1) It is difficult to add a driving mechanism to a small-scale model rotor blade in experimental research, and full-scale experiments are too expensive. (2) Numerical simulations must consider the unique aerodynamic shape of the TEF and model high-order deflection. It is also challenging to simulate the motion between the main blade and the TEF and the flow field near the TEF (such as slot flow [26]) in sufficient detail.

Therefore, the authors combined the advantages of the reverse overset assembly technique (ROAT) [27], arbitrary Lagrangian-Eulerian (ALE) numerical simulation, and experience in AFC airfoil simulation in previous research to establish an AFC rotor numerical model and verify the grid independence. The effect of AFC on the blade surface load is verified. We investigate the effects of the parameters on the flow conditions, TEF size and position, and control performance. Suggestions for AFC rotor design are provided based on the observed phenomena, such as the environmental consistency of the AFC control and resonance amplification.

2. Simulation Method

2.1. The Motion Overset Mesh Method. The grid assembly of the AFC rotor uses the ROAT proposed by the author in a previous study [27]. The AFC rotor grid used in the CFD simulation is obtained by overlapping the main blade grid

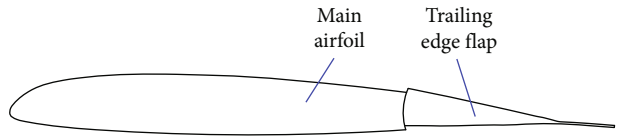

(a)

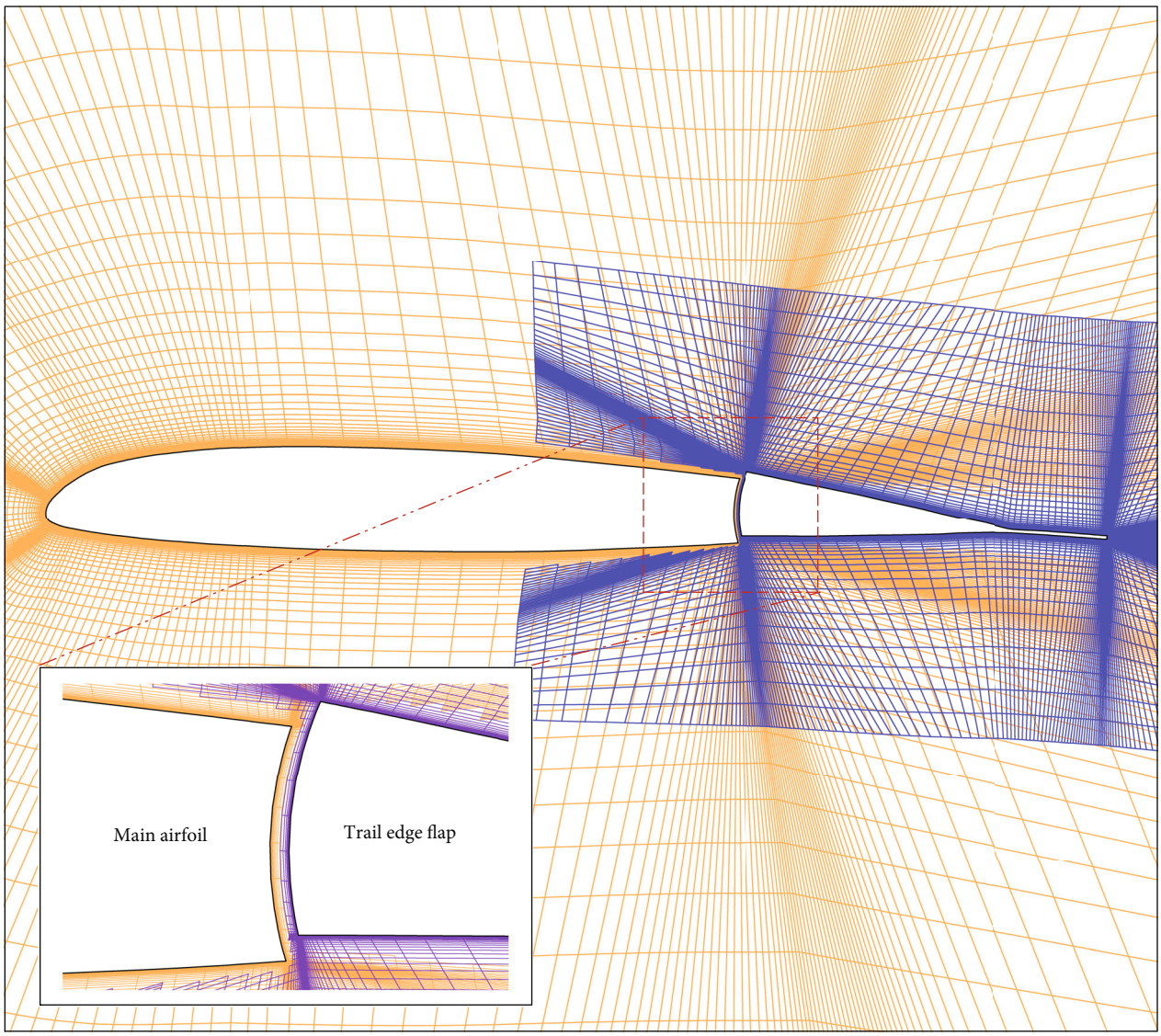

(b)

Figure 3: Continued.

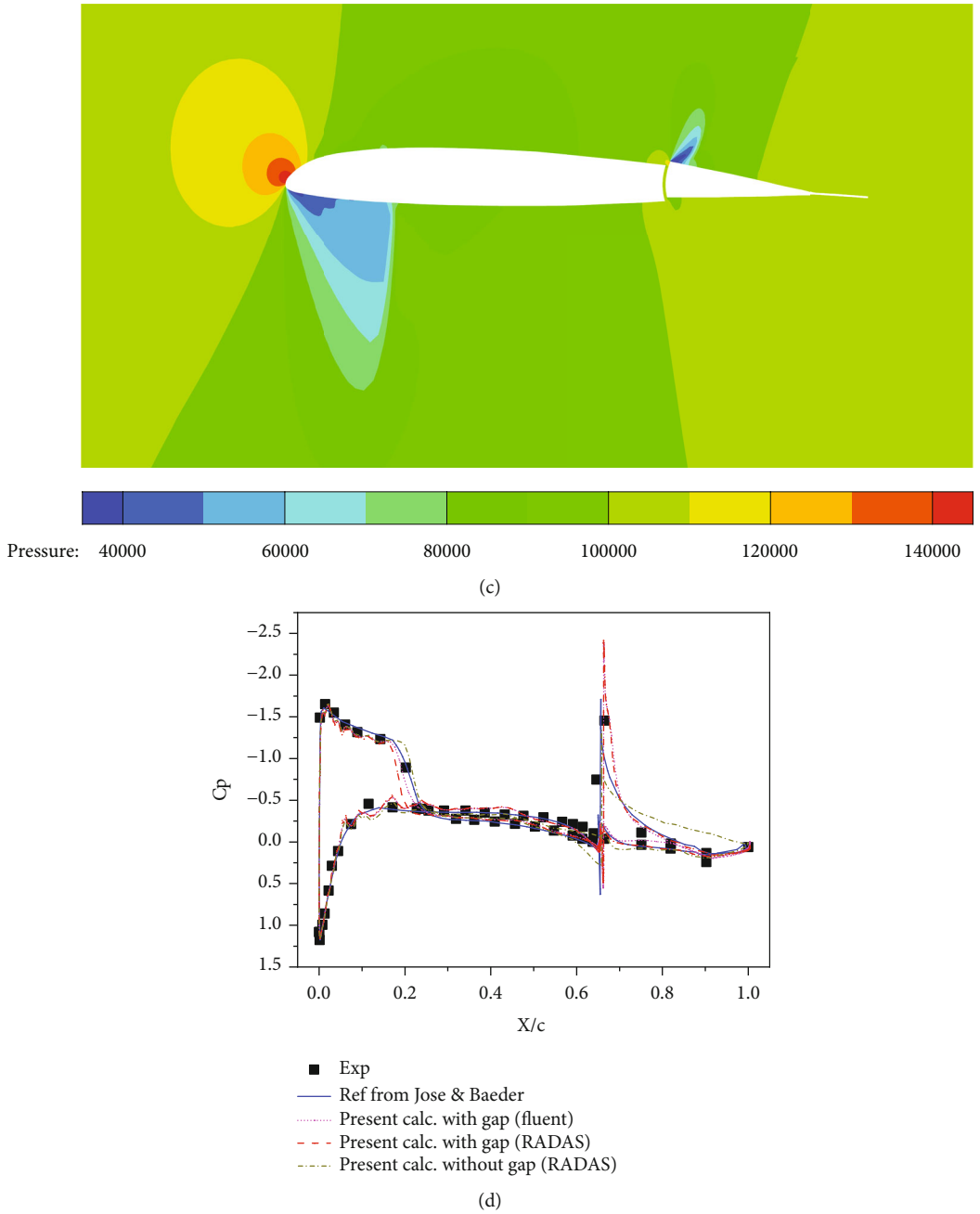

Figure 3: Validation of the AFC airfoil with the HH-06 airfoil: (a) HH-06 airfoil with deflecting TEF; (b) overset grid applied in present simulation; (c) flow field simulation results; (d) comparison of surface pressure coefficients.

and the TEF grid to ensure that the grid near the body follows the TEF's rigid transformation without causing grid deformation, and high grid quality in complex movements is obtained. The main steps of the ROAT method are shown in Figure 2(a). In step 1, the grids are searched to find the donor cells. The cell volume and the wall distance of each cell are compared with that of the donor cell to obtain the initial classification results based on the competition criterion. In step 2, several cells are selected as interpolation cells from the initial classification results according to the user's boundary setting. Finally, in step 3, the final overset assembly result is obtained by combining the donor cell and interpolation cell information. Compared with the deformation mesh technology [16], this strategy can model the gaps in the actual structure, thus giving a more realistic flow field simulation result, and has been verified and applied in our previous research. In addition, a straightforward motion description method of the TEF based on coordinate system transformation is proposed. The concept of this method is that the movement of one coordinate system relative to another can be described by translation and rotation. Complex motion can be converted into ground motion after

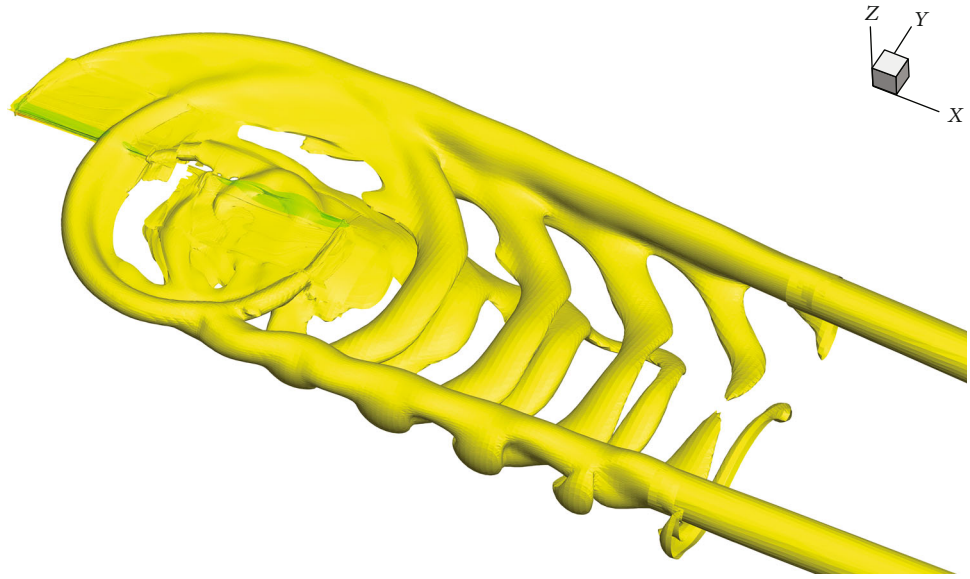

Figure 4: Flow field simulation results of AH-1G rotor in forward flight.

several simple conversions by repeating this step many times, as shown in Figure 2(b) [28]. The coordinate transformation function is shown in equation (1).

$$\begin{aligned}\begin{pmatrix} P'_{1i} \\ P'_{1j} \\ P'_{1k} \end{pmatrix} = &\left(\begin{bmatrix} R_{ii}(t) & R_{ij}(t) & R_{ik}(t) \\ R_{ji}(t) & R_{jj}(t) & R_{jk}(t) \\ R_{ki}(t) & R_{kj}(t) & R_{kk}(t) \end{bmatrix} \right. \\ &\left. \times \begin{bmatrix} ii_{b1} & ij_{b1} & ik_{b1} \\ ji_{b1} & jj_{b1} & jk_{b1} \\ ki_{b1} & jk_{b1} & kk_{b1} \end{bmatrix} \right)^{-1} \begin{bmatrix} ii_{b2} & ij_{b2} & ik_{b2} \\ ji_{b2} & jj_{b2} & jk_{b2} \\ ki_{b2} & jk_{b2} & kk_{b2} \end{bmatrix} \\ &\times \left(\begin{pmatrix} P_{2i} \\ P_{2j} \\ P_{2k} \end{pmatrix} - \begin{pmatrix} b_{2i} \\ b_{2j} \\ b_{2k} \end{pmatrix} \right) + \begin{pmatrix} b_{1i} \\ b_{1j} \\ b_{1k} \end{pmatrix} \\ &+ \begin{pmatrix} T_i(t) \\ T_j(t) \\ T_k(t) \end{pmatrix}, \end{aligned} \tag{1}$$

where $[b_{1i}, b_{1j}, b_{1k}]^T$ and $[b_{2i}, b_{2j}, b_{2k}]^T$ are the coordinates of the reference point b in the two Cartesian coordinate systems O_1 and O_2 involved in the coordinate transformation; $ii_{b1}, ij_{b1}, ik_{b1} \cdots$ and $ii_{b2}, ij_{b2}, ik_{b2} \cdots$ are the basis vectors of reference coordinate systems established at point $b$expressed in O_1 and O_2, respectively; $T(t) = [T_i(t), T_j(t), T_k(t)]^T$ is the translation vector; and $R(t)$ is the matrix of rotation transformation. P'_1 can be calculated by performing the coordinate transformation to P_2 which is in a moving coordinate system. Complex motion, which could be a combination of twisting motion, leading-lagging motion, flapping motion, rotation, etc., can be converted into ground motion after several conversions by repeating this step many times. More detailed information can be found in the patent file [28].

2.2. CFD Method. This paper uses the CFD method based on the unsteady Reynolds-averaged Navier-Stokes equations (URANS) to obtain high accuracy and efficiency. This method, shown in equation (2), is commonly used in rotor flow field simulation.

$$\frac{\partial}{\partial t} \int_V W dV + \int_S [F(W) - G(W)] dS = 0, \tag{2}$$

where $W = [\rho, \rho u, \rho v, \rho w, \rho E]^T$ is the conserved variable, ρ is the density, $\mathbf{u} = [u, v, w]^T$ is the velocity of the flow in a grid cell, E is the total energy per unit mass, and $\boldsymbol{F}(\boldsymbol{W})$ and $\boldsymbol{G}(\boldsymbol{W})$ are the inviscid and viscous fluxes, respectively. The calculations were performed using the rotorcraft aerodynamics and aeroacoustics solver (RADAS) [29]. The ROE-MUSCL (Roe's upwind scheme and monotone upstream-centered schemes for conservation laws) spatial discretization scheme is chosen for the blade grid with the implicit lower-upper symmetric Gauss-Seidel (LU-SGS) temporal discretization and the Spalart-Allmaras (S-A) turbulence model. In contrast, a central differencing scheme is used for the background grid of the AFC rotor and calculated using the inviscid Euler equation. Furthermore, the dual time-stepping scheme is adopted to calculate the load fluctuation in unsteady flow. These settings are consistent with the author's previous research on an AFC airfoil [24], similar to Strawn's research [30], and have been fully verified in rotor simulations.

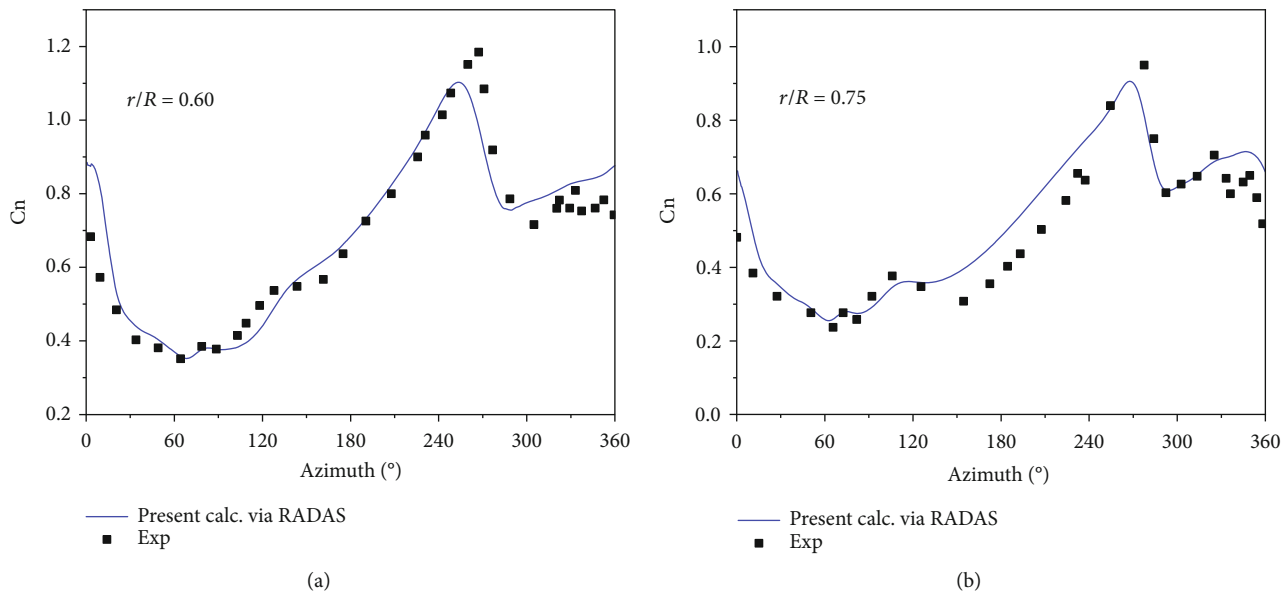

Figure 5: The normal force on the blade of the AH-1G rotor in forward flight: (a) 0.60R; (b) 0.75R.

Table 1: The parameters of the AFC rotor.

Parameter	Value
Rotor radius (R) (m)	1.0
Airfoil	NACA0012
Shape	Rectangular
Number of blades	2
Twist angle (Deg)	0.0
Main blade chord (c) (m)	0.12
TEF chord (c_{tef}) (c)	0.25
TEF length (L_{tef}) (R)	0.18
TEF installation position[1] (R)	0.75

[1]Calculated from the root end face of the TEF.

Table 2: The operating condition parameters of the AFC rotor.

Parameter	Value
Reynolds number (Re)	2.0×10^6
Rotation rate (ω) (rad/s)	40π
Rotation rate (RPM)	1200
Advance ratio (μ)	0.24
Collective pitch angle (Deg)	5.0
Shaft tilt angle (Deg)	1.4

Table 3: The control parameters of the TEF.

Parameter	Value
Frequency (ω_{tef}) (ω)	2.0
Amplitude (A_t) (Deg)	6.0
Phase (φ_{tef}) (Deg)	-120 and 40
Offset (θ_{T_0}) (Deg)	0.0

2.3. Validation of Method

2.3.1. Verification of AFC Airfoil Flow Field. The HH-06 airfoil [20] is used as the verification case. The original airfoil shape and the deflected airfoil are shown in Figure 3(a); the TEF is deflected downward by 4°. The overset grids are shown in Figure 3(b). The cell number of main airfoil is 18 thousand, and the cell number of the TEF is 13.5 thousand, with 10.01 thousand cells in the background. The flow field obtained by the RADAS for the inflow condition of AOA = −4.03° and Ma = 0.758 is shown in Figure 3(c). Figure 3(d) shows the comparison of the surface pressure coefficients obtained from the experiment [20], RADAS, FLUENT software, and Jose and Baeder [18]. The results show that the simulation of the AFC airfoil by the RADAS is of reasonable accuracy.

2.3.2. Verification of AH-1G Rotor's Forward Flight. Figure 4 shows the flow field vorticity results of the AH-1G rotor in forward flight with a tip Mach number of 0.65 and an advance ratio of 0.19. This rotor has two rectangular blades with a chord length of 0.727 m, an aspect ratio of 9.8, and a linear negative twist of -10°/R. In the simulation, the Reynolds number is 9.73×10^6, the rotor pull coefficient is 0.0464, and the trim result is $\theta(\psi) = 6.10 - 5.03 \sin \psi + 1.19 \cos \psi$. The cell number of each main blade is 1.197 million, with 2.56 million cells in the inner background and 3.60 million cells in the outer background. Figure 5 depicts the normal force obtained from the RADAS and an experiment reported by [31] for different radii. The proposed method is suitable for the rotor simulation in forward flight.

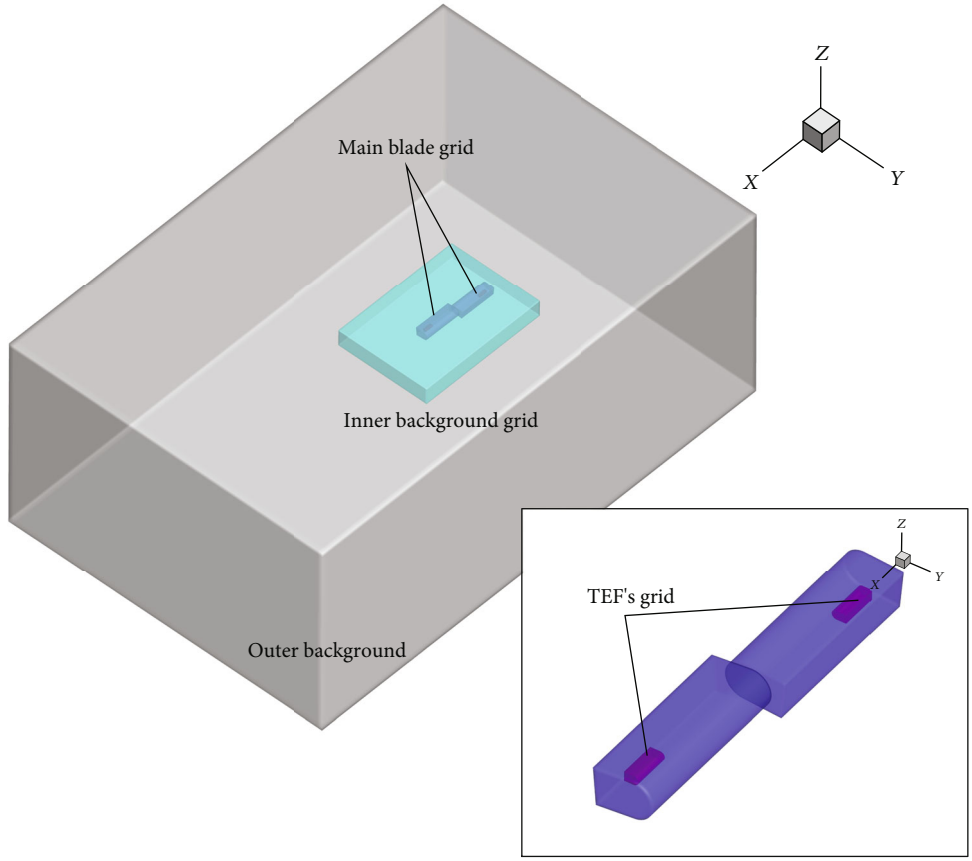

Figure 6: Layout of the simulation grids.

3. Case Study Settings and Analysis

3.1. Model Parameters. A numerical simulation of the 3D AFC rotor is carried out. The change in the TEF deflection angle is calculated by a harmonic oscillation function as shown in equation (3), where θ_t is the deflection angle of the TEF, θ_{T_0} is the offset angle, A_t is the deflection amplitude (the downward deflection is positive), ω_{tef} is the frequency, and φ_{tef} is the phase of control. The AFC rotor's base parameters are listed in Tables 1–3.

$$\theta_t = \theta_{T_0} + A_t \sin\left(\omega_{\text{tef}} t + \varphi_{\text{tef}}\right). \tag{3}$$

The chordwise gap between the TEF and the main blade is 1.0%c, and the spanwise gap is 0.075%R.

3.2. Grid Layout and Overset Assembly. The grid layout is shown in Figure 6, where the incoming flow is in the positive direction of the x-axis. Similar to Aoyama et al.'s research [2] on the rotor blade vortex interaction, there are two Cartesian background grids with different sizes to ensure high accuracy and reduce the overall number of grid points. The dimensions of the coarse outer background are 15R length (x-axis: -5R to 10R), 10R width (y-axis: -5R to 5R), and 6R height (z-axis: -3R to 3R) with 0.48 million cells. The grid resolution in the X and Y directions are 0.096c and 0.025c, respectively. The dimensions of the fine inner background are 3.9R length (x-axis: -1.4R to 2.5R), 2.8R width (y-axis: -1.4R to 1.4R), and 0.5R height (z-axis: -0.25R to 0.25R) with 2.8224 million cells. The blade mesh has a C-H topology, and the overset interpolation boundary of the main blade and TEF is $1c$ and $1c_{\text{tef}}$ from the wall faces in the normal direction. The cell number of each main blade is 1.428 million, and the cell number of the TEF is 0.405 million. The presented overset grid set is considered as the baseline set, and the detailed grid independence verification is applied in the following section.

The assembled grid is shown in Figure 7. The inner background grid is embedded in the outer background grid, and two main blades are embedded in the inner background grid. The main blade grid cells surround the TEF's grid and overlap it. The grid system constitutes an overset grid with multiple overlapping levels.

3.3. Verification of Grid Independence. The grid independence of the uncontrolled AFC rotor is verified. While the topology of the main blade grid remains unchanged, grids with different cell numbers are tested to consider the influence of the blade. Two groups of fine inner background grids are tested to consider the influence of background grid. The size of the baseline inner background grid is 0.096c as group 1, and that of the refined inner background grid is 0.065c as group 2. Similarly, blade grids with different cell numbers are used; the details are listed in Table 4. Thus, as described

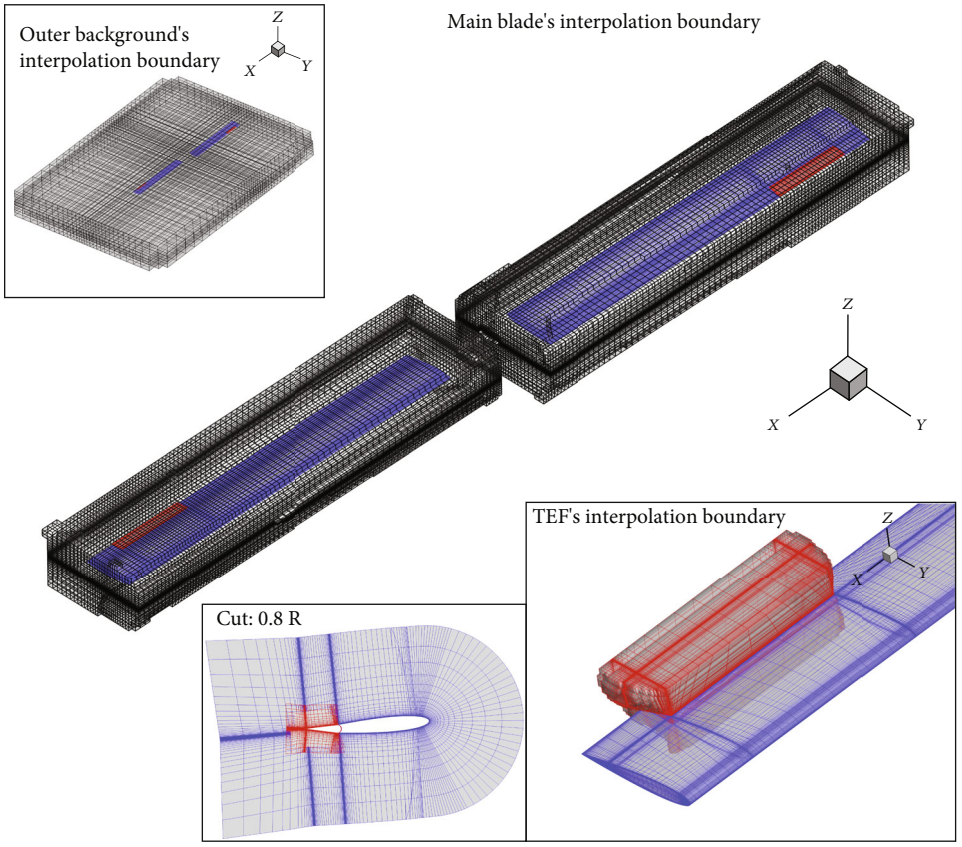

Figure 7: Overset assembly of the AFC rotor grids.

Table 4: Details of blade and background grids for different cell numbers.

Relative cell number of blade grid	Blade grid layout (chordwise, normal-wise, and spanwise)	Background layout (x, y, z) Total cell number (million)	
		Group 1 $191 \times 191 \times 41$	Group 2 $283 \times 283 \times 61$
0.25	$65 \times 23 \times 65$	4.03	—
0.5	$83 \times 29 \times 82$	4.81	11.46
1.0	$101 \times 36 \times 101$	6.10	12.74
2.0	$127 \times 45 \times 127$	8.57	15.22

in Section 3.2, the baseline grid set is with the relative cell number of blade grid of 1 and with group 1 as the inner background grid. The first layer grid of each main blade grid and TEF's grids is $y+ \leq 1$. Figure 8 shows the calculation results for different grid sizes. As shown in Figure 8(a), the peak values of the normal force in the 0.7R section are lower (higher) than the reference baseline for a relative grid size of 0.25 (0.5). The results for a grid size of 2.0 are slightly different from the baseline. There is no apparent difference between group 1 and group 2 with different background grid cells, as shown in Figure 8(b). Therefore, the grid size of 1.0 in group 1, namely, the baseline grid set, selected in this study meets the simulation requirements.

3.4. AFC Control Performance. Figure 9 shows the vertical force distribution of the rotor disk without AFC control and with AFC control for the -120° phase and 40° phase. The parameters of baseline case without AFC control are the same as that listed in Tables 1 and 2, while other AFC parameters listed in Table 3 are set to 0. And the case with AFC control is the same as listed in Tables 1–3. Since there is no trim control, the blade load is the largest in the tip region when the azimuth angle is 90° and the smallest in the root region when the azimuth angle is 270° without AFC control, as shown in Figure 9(a). For the AFC control with the -120° phase, the TEF deflection frequency is 2ω (denoted as 2P); thus, the TEF is downward deflected near

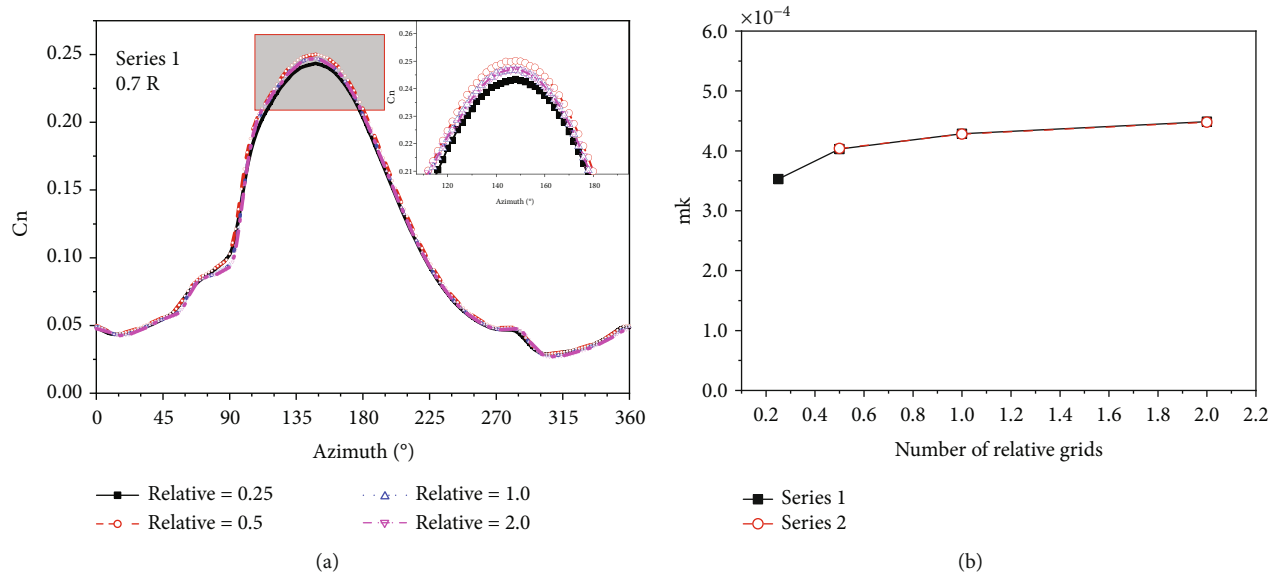

Figure 8: Comparison of rotor aerodynamic results for different grid sizes: (a) normal force coefficient of 0.7R; (b) torque coefficient.

the 90° azimuth, increasing the thrust of the blade. In contrast, the TEF is upward deflected in the 40° phase control case, reducing the blade's thrust. The vertical force is similar for the -120° phase control and no control but substantially different for the 40° phase control.

Figure 10 shows the vertical force of the 0.8R section. Figure 10(a) shows the vertical force for different azimuth angles, and Figure 10(b) shows its change rate with respect to the azimuth angle. The change rate of the vertical force is significantly different for the cases with and without AFC control. According to Lighthill's acoustic analogy and Farassat's formulation 1A [32], the load and its time derivative, namely, the force and its change rate, determine the loading noise of the rotor. As can be seen in Figures 9 and 10, the AFC control can introduce significant change in the distribution of the force and its change rate. A properly selected AFC control parameter could have the potential to decrease the overall load or its change rate and lead to a noise reduction, such as the control phase of 40° shown in Figure 10.

4. Parameter Analysis and Discussion

As described in Section 3.1, the parameters of baseline case without AFC are the same as that listed in Tables 1 and 2, while other AFC parameters listed in Table 3 are set to 0. And the parameters of the two baseline cases with AFC control are the same as listed in Tables 1–3, with a control phase of -120° or 40°, respectively. In the following sections, all the parameter analysis cases are based on the baseline cases. Only the parameter to be studied is changed, while other parameters remain to be identical to the baseline cases. The two control phases of baseline cases with AFC are selected to show possible influence of AFC parameters for different control phases.

4.1. Operation and Flow Condition

4.1.1. Rotational Speed and Advance Ratio. Different advance ratios and rotational speeds (20π, 40π, and 60π rad/s) are tested to evaluate the performance of the AFC rotor under different operating conditions. The thrust coefficient and torque coefficient are shown in Figure 11. The rotor thrust coefficient and torque coefficient increase with the advance ratio and rotational speed because the maximum speed on the advancing side of the blade is only about Ma = 0.72 at a maximum advance ratio of 0.32 and a rotational speed of 60π rad/s. No wide range stall which could lead to obvious aerodynamic performance loss occurs. The thrust and torque coefficients are slightly smaller for -120° phase control than without AFC control. Although the thrust is slightly higher at 40° phase control than without AFC control, the torque coefficient is significantly different, i.e., higher at 20π rad/s and lower at 60π rad/s. In general, the difference in thrust between with and without AFC control is about 1%. It is slightly higher at high advance ratios. The torque coefficient exhibits a similar phenomenon. The cases at a given rotation speed with a certain AFC control and without AFC control exhibit a constant torque coefficient offset at the advance ratio over 0.15. And the torque offset is different under various rotation speed and for different control phases. It can be concluded that at the advance ratio over 0.15, each set of AFC control will introduce a specific resistance offset which is affected by the rotation speed to the rotor and lead to a specific difference in the torque coefficient.

4.1.2. Collective Pitch. Figure 12 shows the rotor thrust coefficient and torque coefficient at collective pitch angles of 4° to 8°. Similarly, the rotor's thrust coefficient and torque coefficient increase with the collective pitch angle, and the thrust coefficient increases almost linearly. No wide range

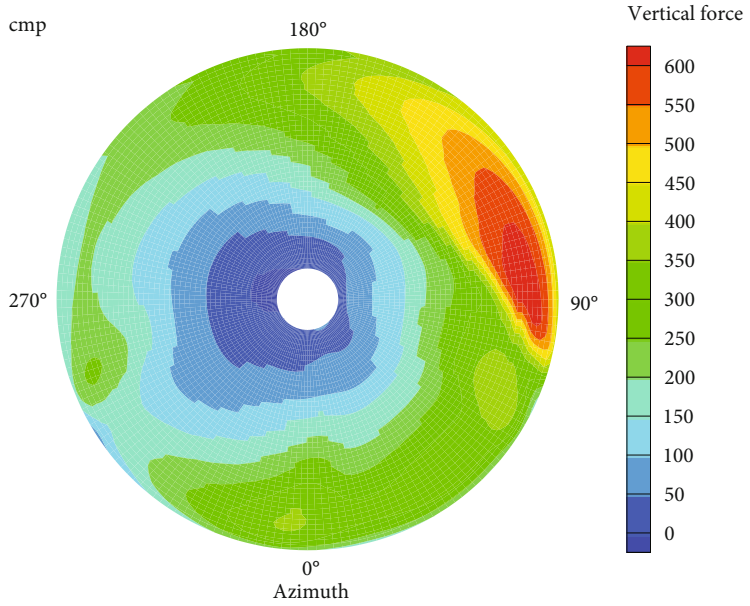

(a)

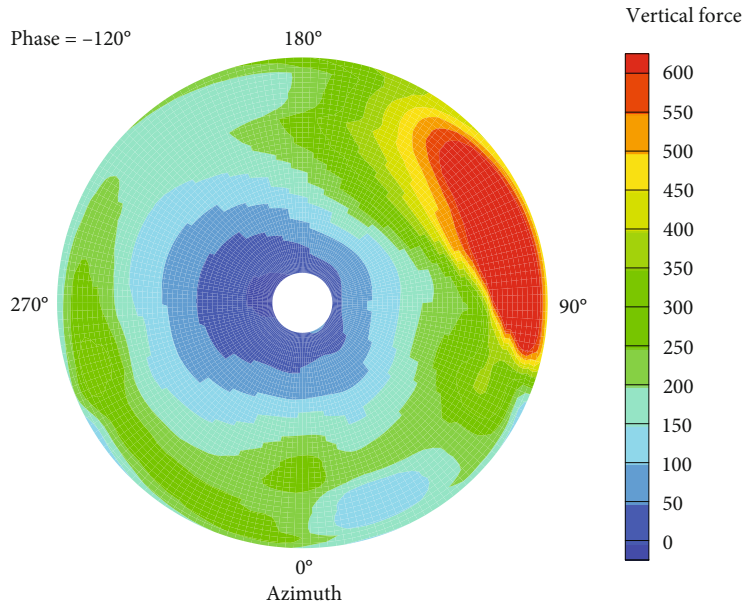

(b)

Figure 9: Continued.

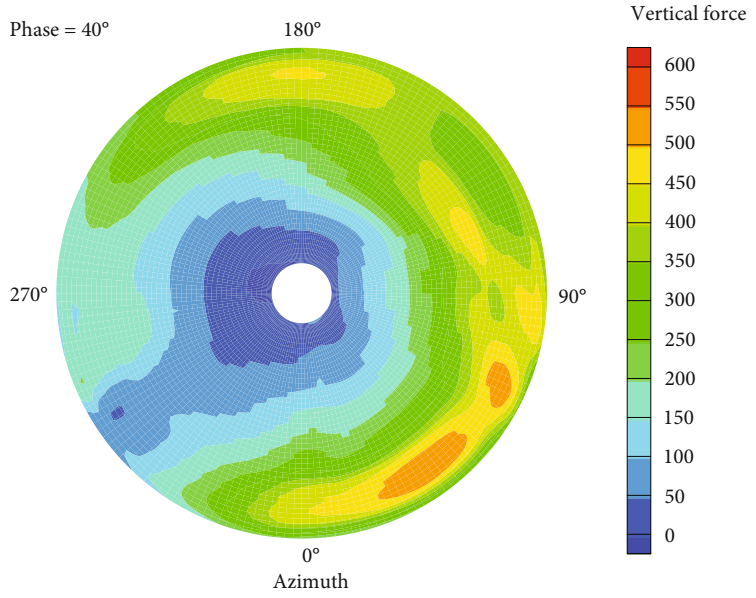

(c)

Figure 9: Vertical force distribution of the rotor with or without AFC control: (a) without control; (b) with control, -120° phase; (c) with control, 40° phase.

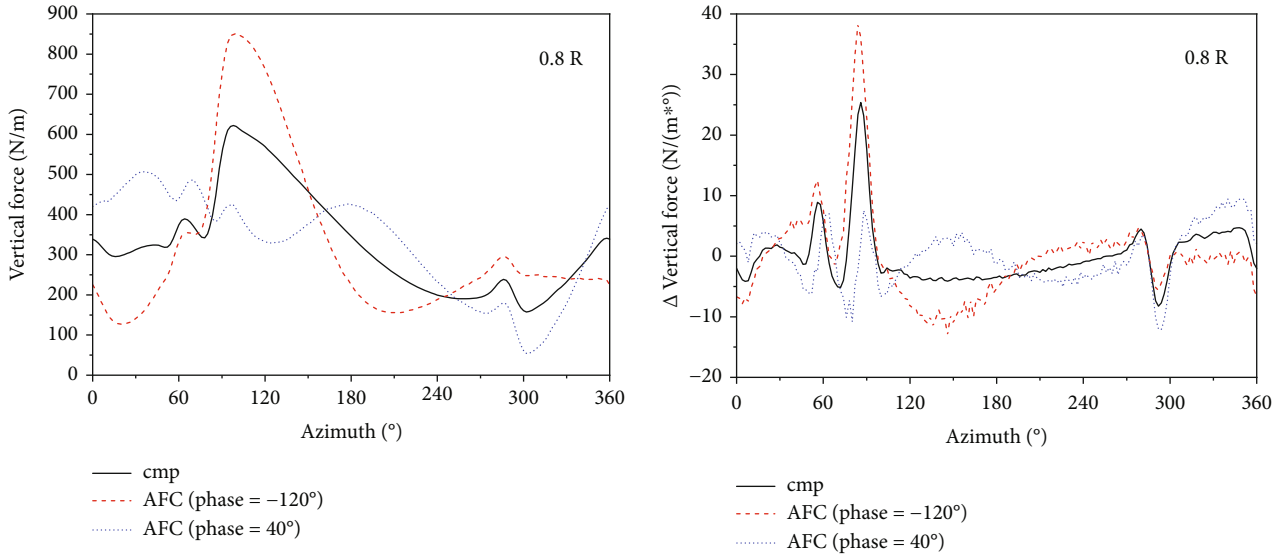

(a) (b)

Figure 10: Vertical force of 0.8R section with or without AFC control: (a) vertical force of 0.8R section; (b) change rate of vertical force.

stall occurs. The rate of rise of the torque coefficient increases with the pitch angle. The changes in the thrust and torque coefficients are generally similar to those of a conventional rotor [33]. Furthermore, the difference in the parameter values between AFC control and no control does not change significantly with an increase in the collective pitch angle.

4.2. TEF Size and Position

4.2.1. Chord Length of TEF. Figure 13 shows the thrust coefficient and torque coefficient for different TEF chord lengths (0.15c, 0.2c, 0.25c, 0.3c, and 0.35c). As the TEF's chord length increases, the thrust coefficient decreases slightly, as shown in Figure 13(a). The reason is that an increase in the chord length increases the peak value of the instantaneous thrust, whereas the thrust decreases in other conditions (such as the upward deflection time), as shown in Figure 14. As depicted in Figure 14(a), the TEF is not always in a downward deflection on the advancing side; thus, the vertical force does not show an increasing trend all the time and the thrust coefficient value changes by 1%. As the chord length increases, the torque coefficient increases slightly

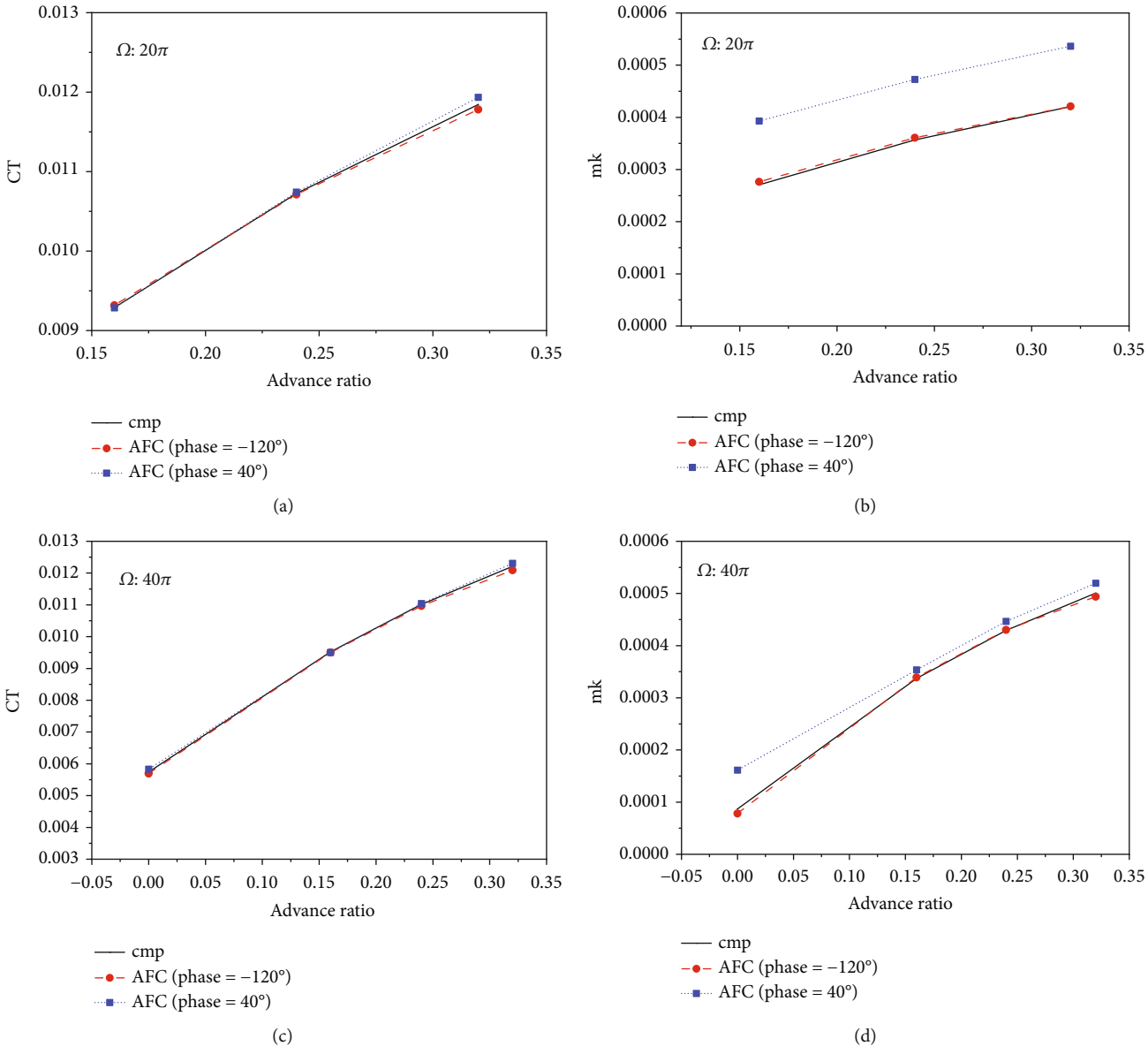

Figure 11: Continued.

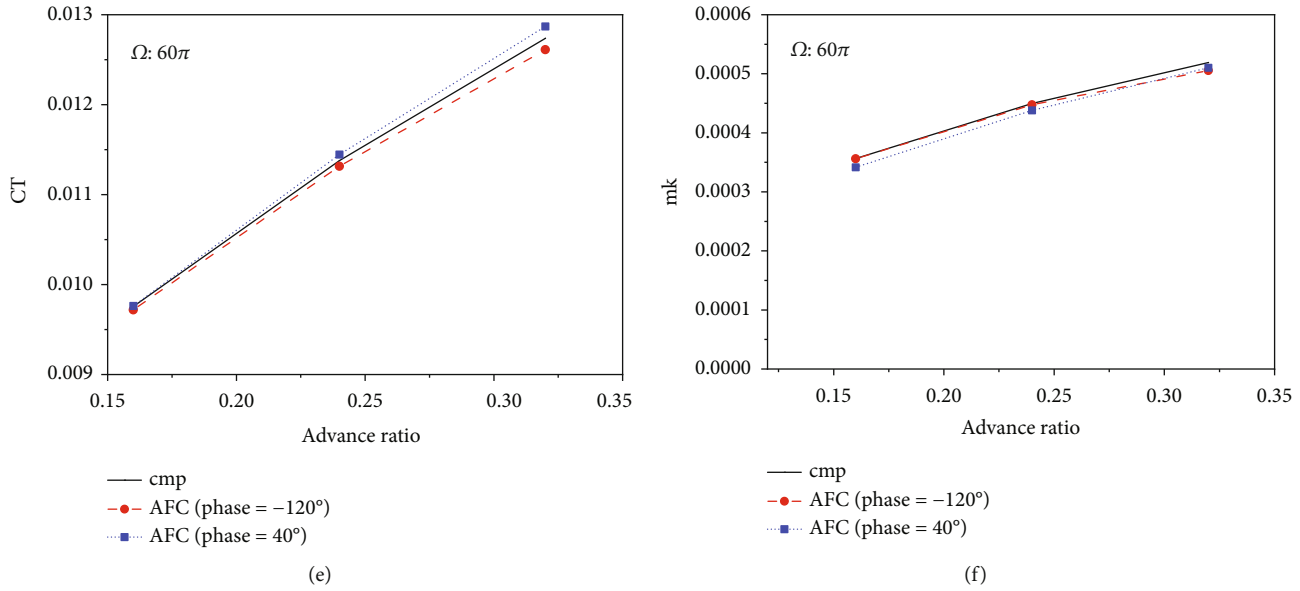

Figure 11: Effect of advance ratio and rotational speed on AFC rotor performance: (a) thrust coefficient at $\Omega = 20\pi$ rad/s; (b) torque coefficient at $\Omega = 20\pi$ rad/s; (c) thrust coefficient at $\Omega = 40\pi$ rad/s; (d) torque coefficient at $\Omega = 40\pi$ rad/s; (e) thrust coefficient at $\Omega = 60\pi$ rad/s; (f) torque coefficient at $\Omega = 60\pi$ rad/s.

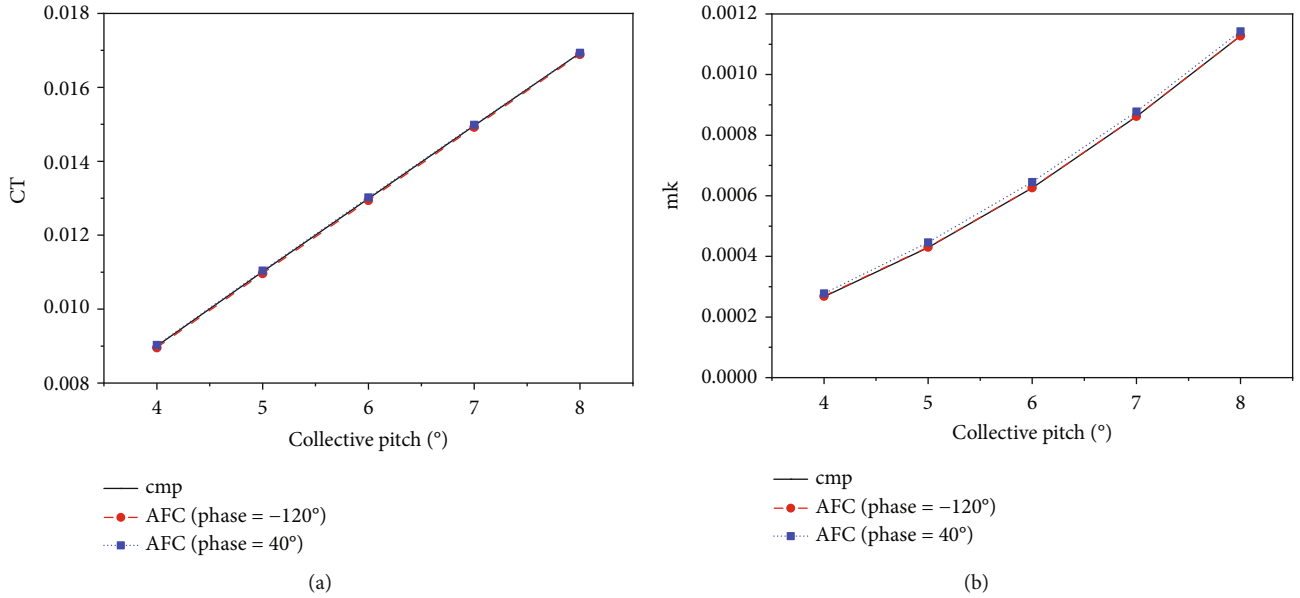

Figure 12: Effect of collective pitch on the AFC rotor: (a) thrust coefficient; (b) torque coefficient.

(from 0.15c to 0.25c) and then decreases. The reason is that the deflection of the TEF increases the drag. However, the TEF's continuous up and down deflection provides a driving force, as shown in Figure 15. In the rotor frame, the horizontal force is "drag" that contributes to the torque when it is positive and in the opposite direction to that of rotation and is "driving force" that counteracts the torque when it is negative and in the same direction with that of rotation. As the TEF chord length increases, the driving force increases, and the torque coefficient decreases. Similar phenomena were also observed in the reference [21] and the author's previous research on AFC airfoils.

4.2.2. The Span Length of TEF. The inner end face of the TEF remained the same, and the span length (0.09R, 0.12R, 0.15R, 0.18R, and 0.21R) was adjusted. Similar to the results for an increase in the chord length, the rotor thrust coefficient decreases slightly due to the disturbance of the flow field by the TEF, but the change is relatively small (within 1%), as shown in Figure 16(a). However, unlike the

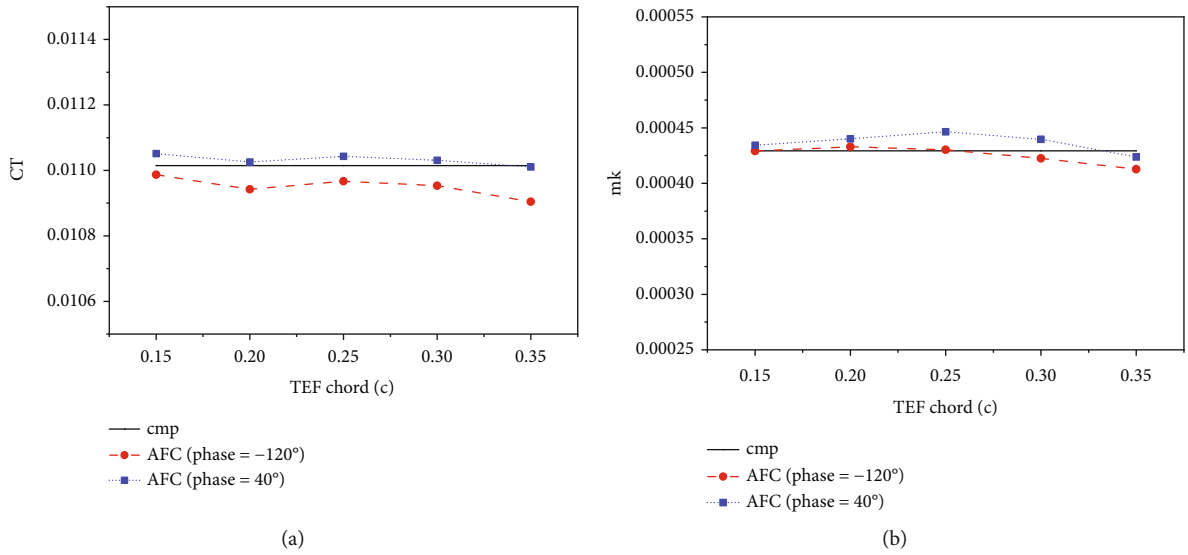

Figure 13: Effect of the TEF chord size on AFC rotor performance: (a) thrust coefficient; (b) torque coefficient.

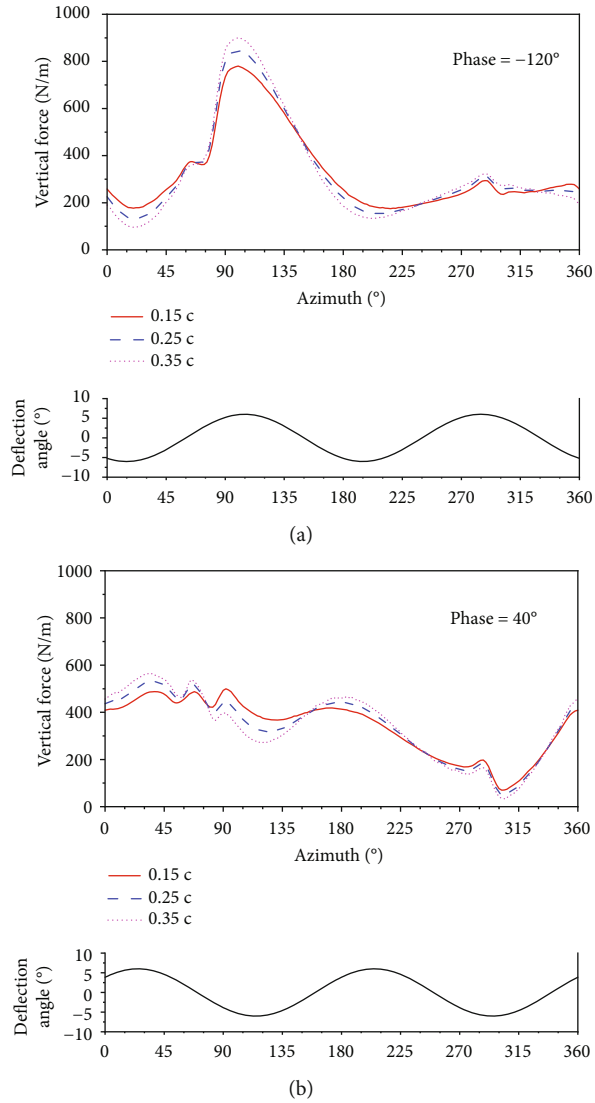

Figure 14: Vertical force of 0.84R section: (a) phase = −120 ∘ ; (b) phase = 40 ∘ .

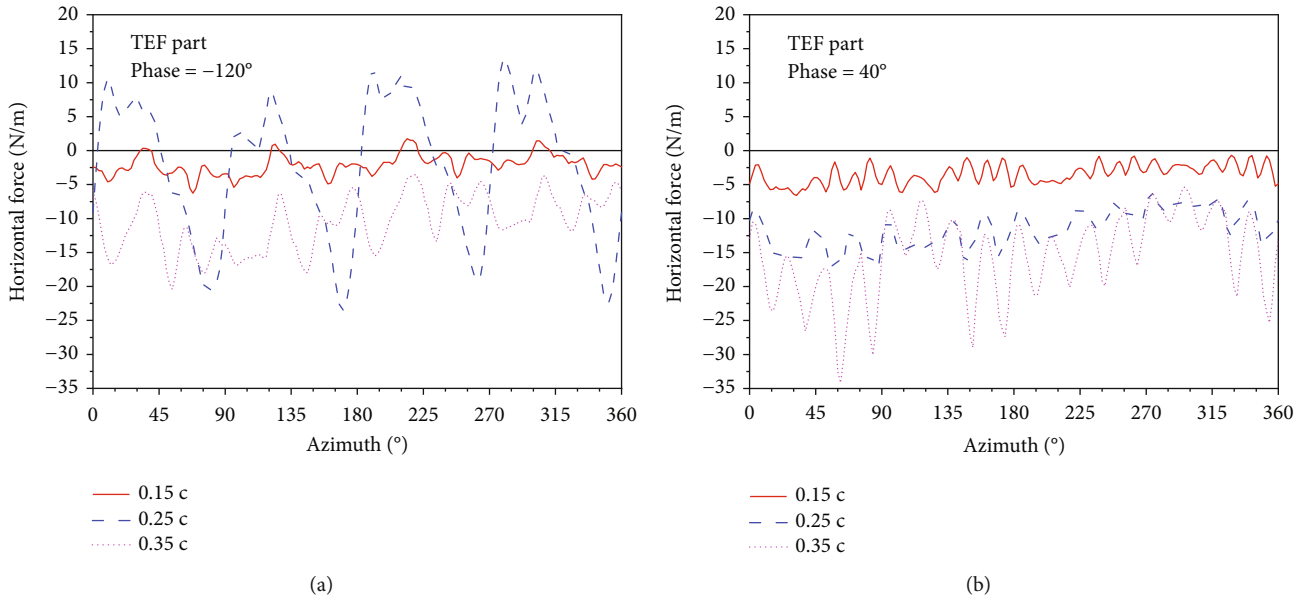

Figure 15: Horizontal force of 0.84R section for different TEF chord lengths: (a) phase = −120 ∘ ; (b) phase = 40 ∘ .

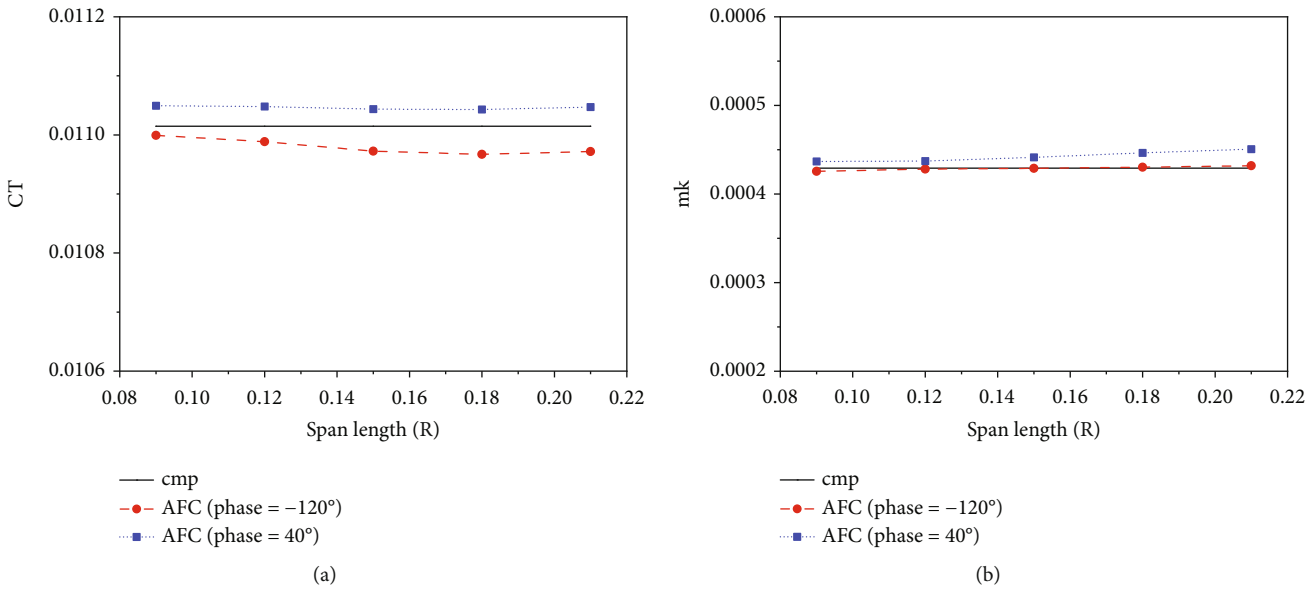

Figure 16: Effect of TEF span length on AFC rotor performance: (a) thrust coefficient; (b) torque coefficient.

results for increasing the chord length, the rotor torque coefficient slowly increases with the span length. The change in the driving force is smaller when the span length increases than when the chord length increases due to an increase in drag because of the TEF, as shown in Figure 17 and compared with Figure 15.

4.2.3. The Span Position of TEF. Figure 18 shows the effect of the TEF installation position (0.65R, 0.7R, 0.75R, and 0.8R) on the rotor's aerodynamic characteristics. As the installation position moves toward the rotor tip, the difference in the thrust coefficient between AFC control and no AFC control decreases. The thrust coefficient increases with the TEF installation position for the -120° phase control and is lower than that in the uncontrolled case. It shows a gradual downward trend for the 40° phase control while the thrust coefficient is higher than that in the uncontrolled case. The reason is that the high-thrust area of the rotor decreases as the TEF installation position moves to the rotor tip (Figure 19). In the -120° phase control case, the root side region of the TEF compensates for the thrust loss when the TEF is installed near the tip; however, this phenomenon is not

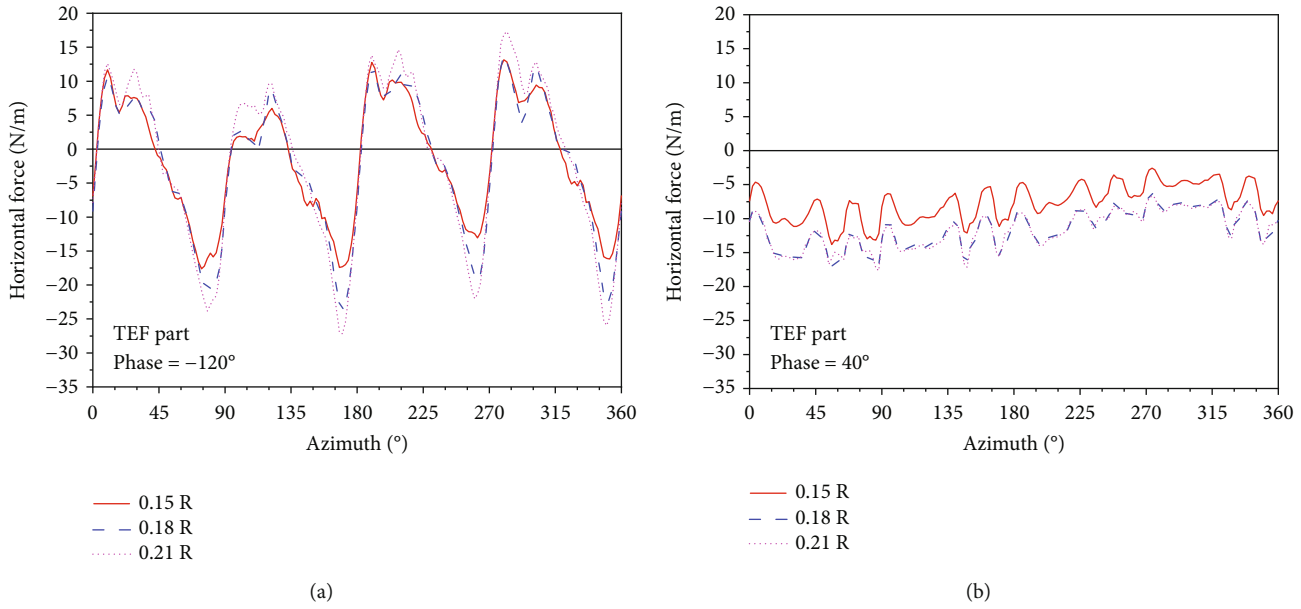

Figure 17: Horizontal force of 0.84R section with different TEF span lengths: (a) phase = −120 ∘ ; (b) phase = 40 ∘ .

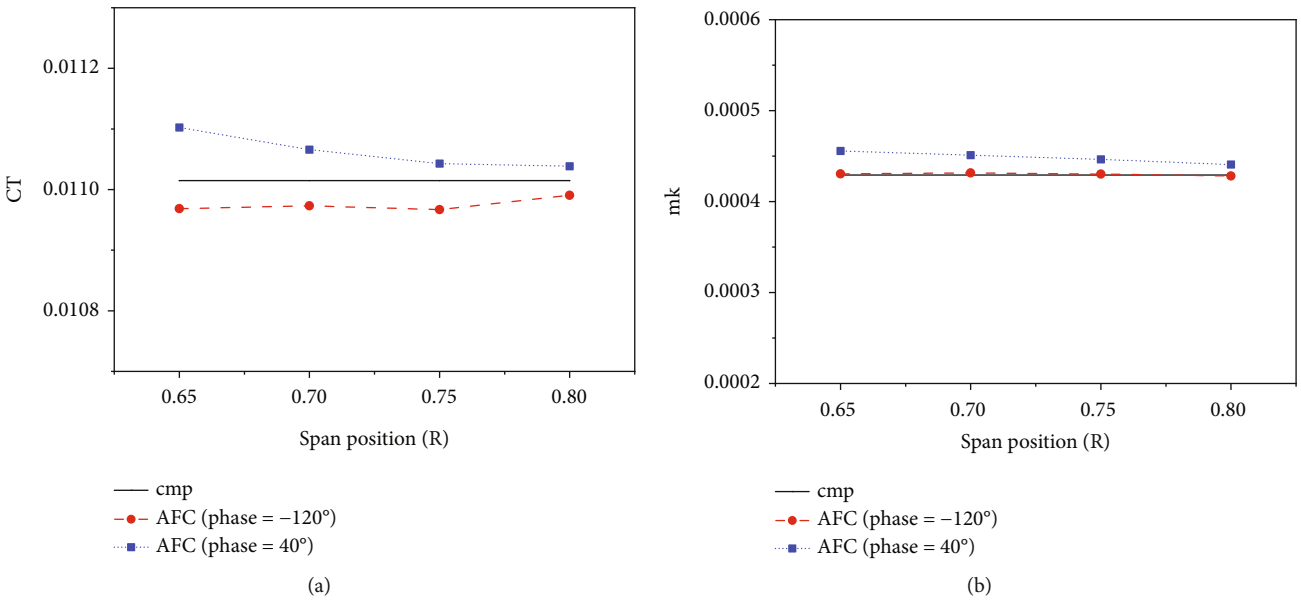

Figure 18: Effect of TEF installation position on AFC rotor performance: (a) thrust coefficient; (b) torque coefficient.

observed for the 40° phase control. The driving force is the highest, and the torque coefficient is the lowest when the TEF is installed near the tip.

4.3. AFC Control Parameters

4.3.1. Frequency and Phase. Studies have demonstrated that the phase is the key factor of AFC control, but it is closely related to the deflection frequency. The effects of the TEF frequency (1P to 4P) and the phase on AFC rotor performance are shown in Figure 20. The thrust coefficient and torque coefficient are significantly larger at a TEF deflection frequency of $k\omega$ (the product of the blade number and the rotation frequency, e.g., 2P and 4P in the test cases), than at other frequencies. When the frequency of the flow field disturbance due to deflection is a multiple of the rotation frequency, stable superposition occurs, resulting in a significant change in the aerodynamic force and a resonance phenomenon. The peak-to-peak value is larger at 2P than that at 4P. As the deflection frequency increases, the trend of the torque coefficient is similar to that of the thrust coefficient. However, it should be noted that the phases required to reach the peak of the thrust or torque coefficient differ for different frequencies. Further analysis is required to obtain the optimum phase.

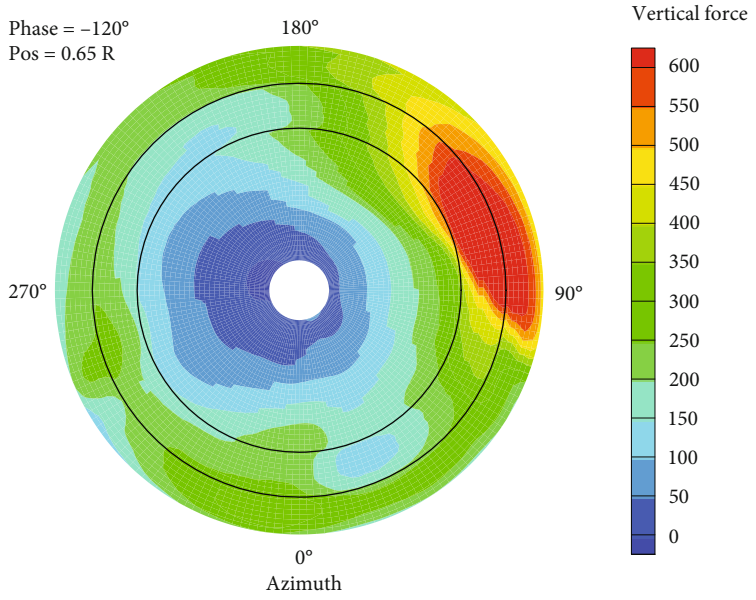

(a)

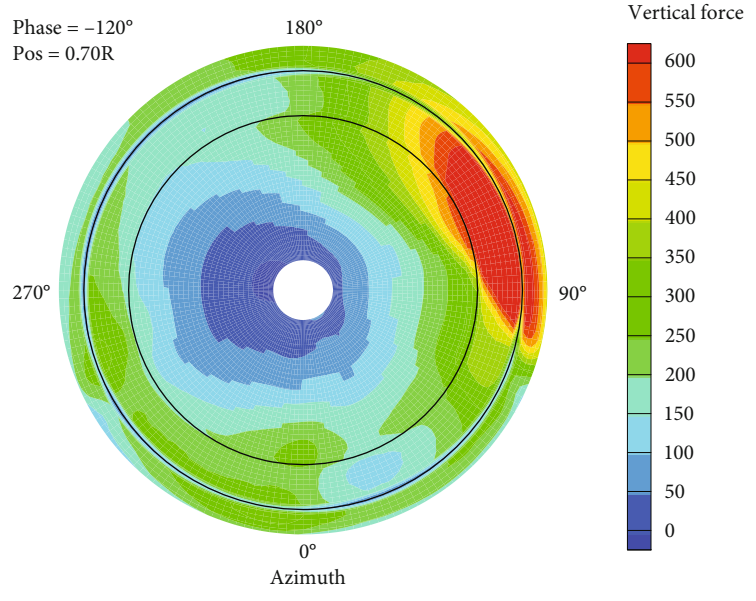

(b)

Figure 19: Continued.

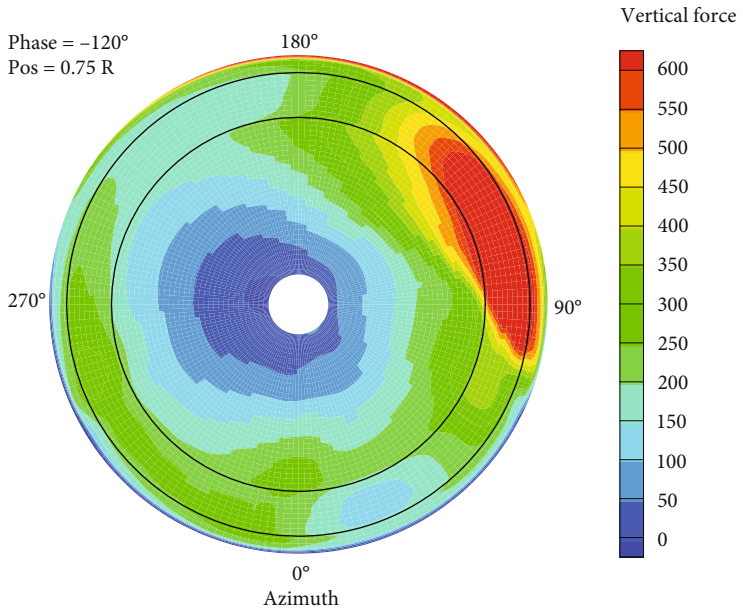

(c)

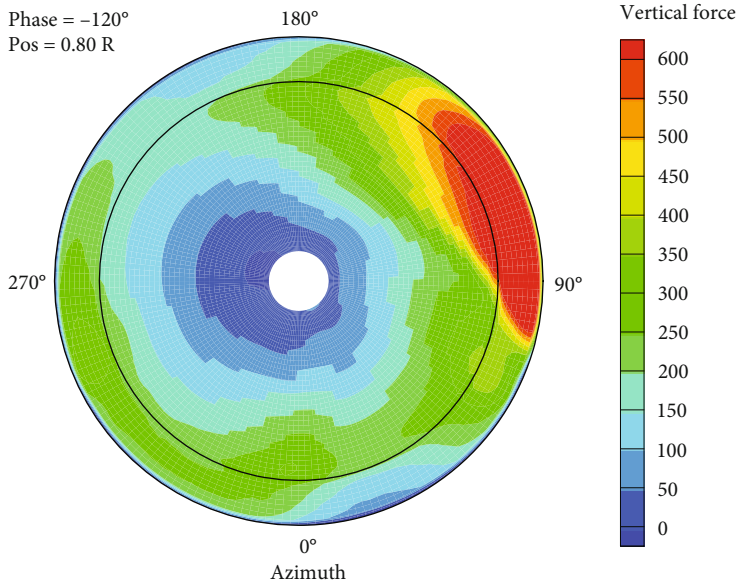

(d)

Figure 19: Continued.

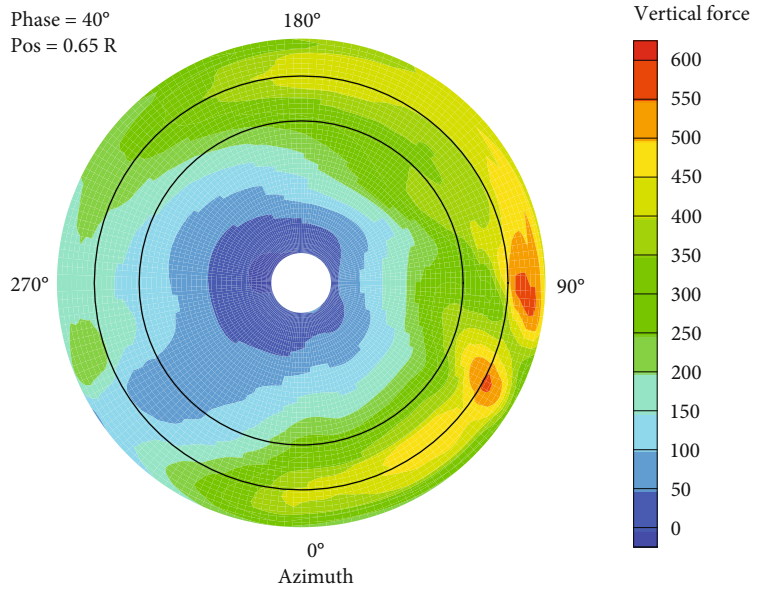

(e)

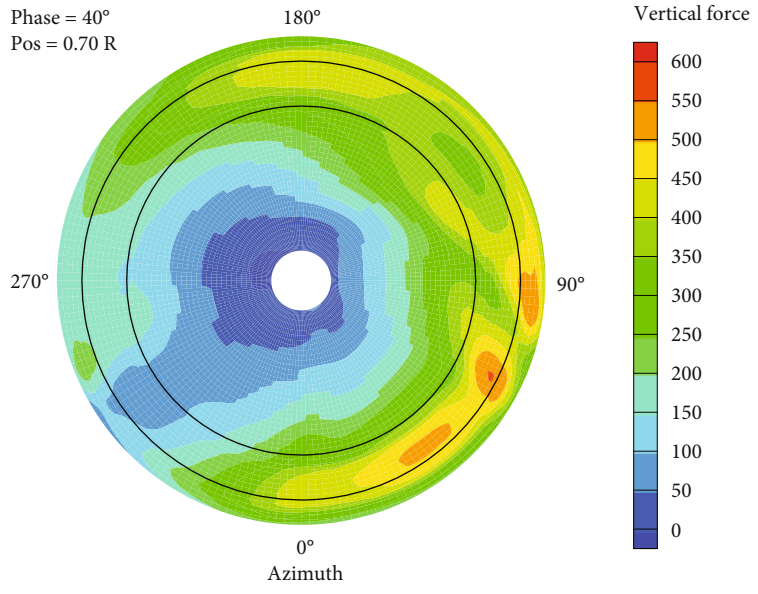

(f)

Figure 19: Continued.

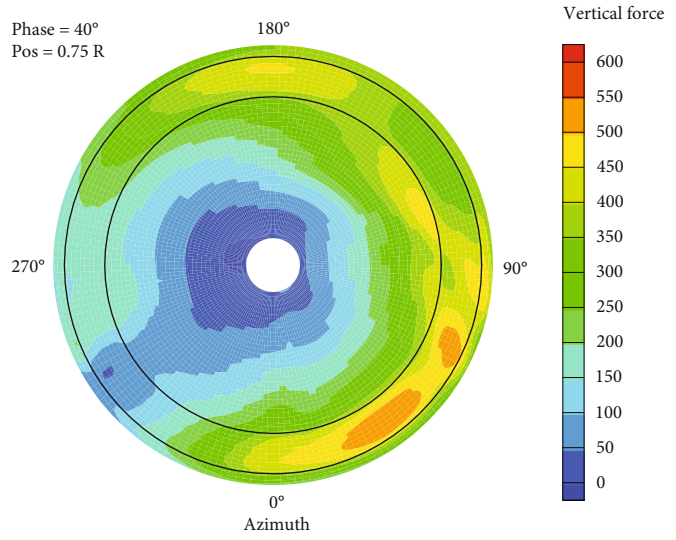

(g)

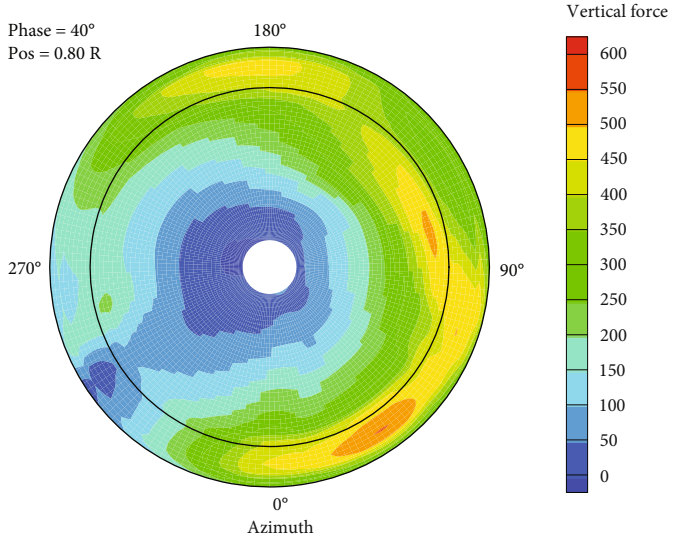

(h)

Figure 19: Vertical force distribution of the AFC rotor disk for different TEF installation positions: (a) TEF at 0.65R, phase = −120 ∘ ; (b) TEF at 0.7R, phase = −120 ∘ ; (c) TEF at 0.75R, phase = −120 ∘ ; (d) TEF at 0.8R, phase = −120 ∘ ; (e) TEF at 0.65R, phase = 40 ∘ ; (f) TEF at 0.7R, phase = 40 ∘ ; (g) TEF at 0.75R, phase = 40 ∘ ; (h) TEF at 0.8R, phase = 40 ∘ .

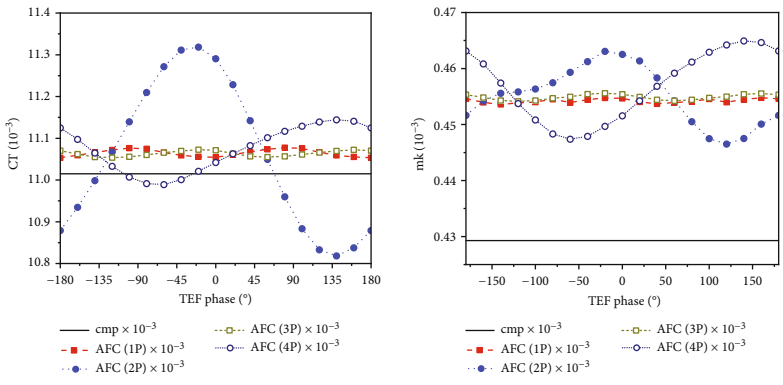

(a) (b)

Figure 20: Effects of TEF frequency and phase on AFC rotor performance: (a) thrust coefficient; (b) torque coefficient.

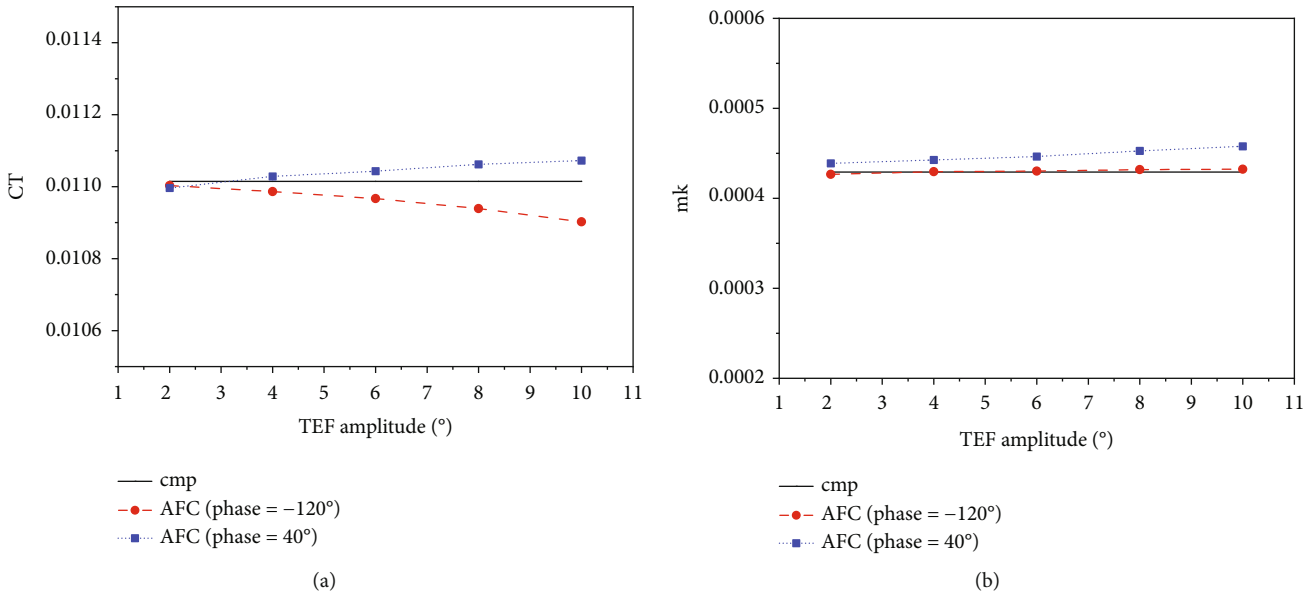

Figure 21: Effect of TEF amplitude on AFC rotor performance: (a) thrust coefficient; (b) torque coefficient.

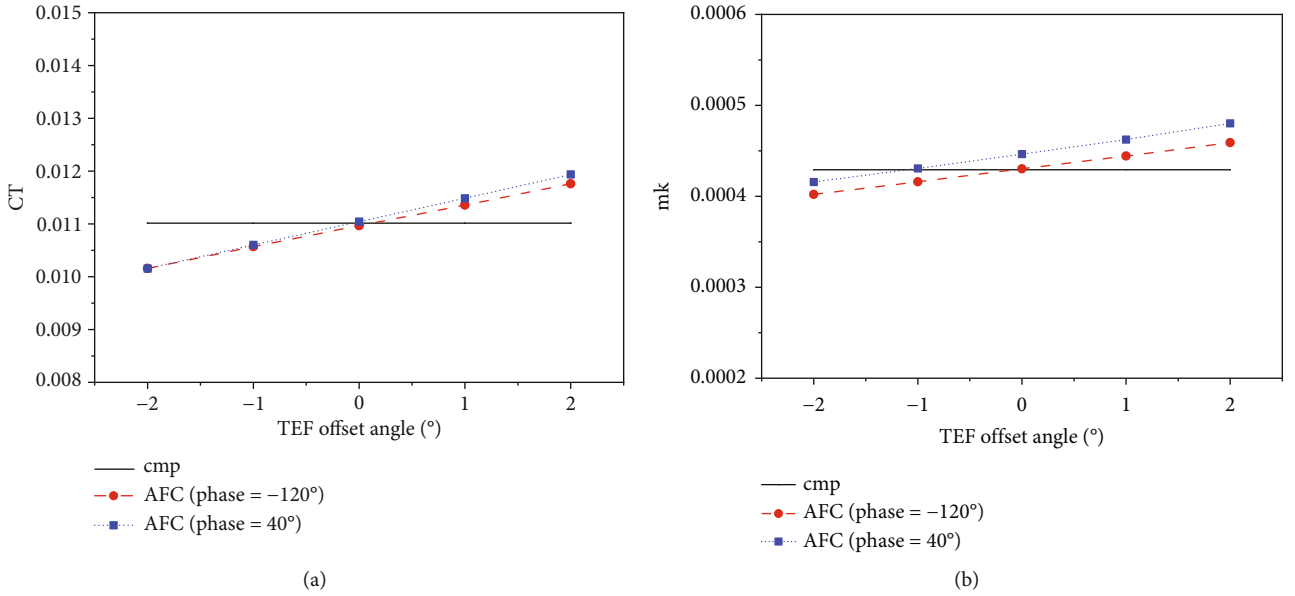

Figure 22: Effect of TEF offset angle on AFC rotor performance: (a) thrust coefficient; (b) torque coefficient.

4.3.2. Amplitude. Figure 21 shows the thrust coefficient and torque coefficient for different TEF amplitudes (2, 4, 6, 8, and 10°). In contrast to the response of the thrust coefficient to the installation position close to the tip, the thrust coefficient decreases as the TEF amplitude increases for the -120° phase but increases for the 40° phase, as shown in Figure 21(a). The reason is that the force of the TEF deflection decreases for the -120° phase case and increases for the 40° phase case. An increase in the deflection amplitude strengthens this effect. Moreover, unlike the thrust coefficient, the torque coefficient increases with the TEF amplitude due to additional drag, regardless of the direction of TEF deflection (Figure 21(b)). The trend is similar to the -120° phase case and the uncontrolled case.

4.3.3. Offset Angle. Figure 22 shows the thrust coefficient and torque coefficient for different TEF offset angles (-2, -1, 0, 1, and 2°). Since the offset angle only changes the average deflection angle of the TEF, the response is similar to an increase in the camber of the airfoil. Thus, the phenomenon is similar to that of the AFC airfoil [34]. An increase in the TEF offset angle results in a linear increase in the thrust coefficient and torque coefficient of the rotor (Figure 22).

5. Conclusion

An AFC rotor with a TEF was simulated using the overset assembly method, multiple coordinate systems, and the URANS solver. The accuracy and suitability of the method were verified. The effect of different operating conditions, TEF size and position, and the control parameters of the rotor were analyzed. The following conclusions were obtained, serving as a reference for the design of AFC rotors.

(1) The deflection of the TEF was equivalent to changing the camber of the airfoil, causing a change in load distribution and significantly influencing the change rate of the vertical force. In general, the deflection of the TEF reduced the thrust coefficient by about 1%, but the appropriate offset angle can compensate for the thrust loss. Hence, multiple purposes, such as optimization of rotor load distribution and significant reduction of vibration and noise, can be achieved by the application of the TEF control with limited penalty in thrust loss with a considerable flexibility compared with passive control methods

(2) With AFC control, the trend of the rotor thrust and torque coefficients for different operating conditions was highly similar with that of conventional rotors. The influence of a certain set of AFC control parameters showed a predictable pattern for a certain rotor under various flight conditions. Therefore, universal design solutions of AFC parameters for a certain rotor should exist for given purposes

(3) The control phase and frequency were the key factors affecting the thrust and torque coefficients. Changes in the thrust and torque were more significant at rotor harmonics with multiple of blade number, approximate to a resonance effect, which can be exploited in AFC rotor design

(4) The deflection of the TEF increased the driving force, reducing the rotor power at large chord and span lengths (but may increase the power of TEF's deflection). As the chord length, span length, and amplitude increased, the change rate of the thrust and torque coefficients increased

Data Availability

The data used to support the findings of this study are available from the corresponding author upon request.

Conflicts of Interest

The authors declare that there is no conflict of interest regarding the publication of this paper.

Acknowledgments

This research was supported by the National Key Laboratory Foundation of China (ID: 6142202202), the Excellent Postdoctoral Program of Jiangsu Province, and the Priority Academic Program Development of Jiangsu Higher Education Institutions (PAPD).

References

[1] B. W. Sim, R. D. Janakiram, and B. H. Lau, "Reduced in-plane, low-frequency noise of an active flap rotor," *Journal of the American Helicopter Society*, vol. 59, no. 2, pp. 1–17, 2014.

[2] T. Aoyama, C. Yang, and S. Saito, "Numerical analysis of active flap for noise reduction using moving overlapped grid method," *Journal of the American Helicopter Society*, vol. 52, no. 3, pp. 189–200, 2007.

[3] F. K. Straub, V. R. Anand, T. S. Birchette, and B. H. Lau, "SMART rotor development and wind tunnel-test," in *35th European Rotorcraft Forum*, pp. 413–430, Hamburg, Germany, 2009.

[4] J. B. Maurice, F. A. King, and W. Fichter, "Derivation and validation of a helicopter rotor model with trailing-edge flaps," *Journal of Guidance, Control, and Dynamics*, vol. 36, no. 5, pp. 1375–1387, 2013.

[5] J. Bain, M. Potsdam, L. Sankar, and K. S. Brentner, "Aeromechanic and aeroacoustic predictions of the Boeing SMART rotor using coupled CFD/CSD analysis," in *The American Helicopter Society 66th Annual Forum*, pp. 106–123, Phoenix, Arizona, USA, 2010.

[6] F. K. Straub, D. K. Kennedy, A. D. Stemple, V. R. Anand, and T. S. Birchette, "Development and whirl tower test of the SMART active flap rotor," in *Symposium on Smart Structures and Materials*, pp. 202–212, San Diego, CA, USA, 2004.

[7] D. Roth, B. Enenkl, and O. Dieterich, "Active rotor control by flaps for vibration reduction - full scale demonstrator and first flight test results," in *32nd European Rotorcraft Forum*, pp. 801–814, Maastricht, The Netherlands, 2006.

[8] M. H. Chia, K. Duraisamy, A. K. Padthe, and P. P. Friedmann, "Active and passive helicopter noise reduction using the AVINOR/HELINOIR code suite," *Journal of Aircraft*, vol. 55, no. 2, pp. 727–740, 2018.

[9] K. Ravichandran, I. Chopra, B. E. Wake, and B. Hein, "Trailing-edge flaps for rotor performance enhancement and vibration reduction," *Journal of the American Helicopter Society*, vol. 58, no. 2, pp. 1–13, 2013.

[10] M. K. McWilliam, T. K. Barlas, H. A. Madsen, and F. Zahle, "Aero-elastic wind turbine design with active flaps for AEP maximization," *Wind Energy Science*, vol. 3, no. 1, pp. 231–241, 2018.

[11] J. Smit, L. O. Bernhammer, S. T. Navalkar, L. Bergami, and M. Gaunaa, "Sizing and control of trailing edge flaps on a smart rotor for maximum power generation in low fatigue wind regimes," *Wind Energy*, vol. 19, no. 4, pp. 607–624, 2016.

[12] A. Altmikus, A. Dummel, R. Heger, and D. Schimke, "Actively controlled rotor: aerodynamic and acoustic benefit for the helicopter today and tomorrow," in *34th European Rotorcraft Forum*, vol. 2, pp. 1373–1420, Liverpool, UK, 2008.

[13] F. K. Straub, D. K. Kennedy, D. B. Domzalski et al., "SMART material-actuated rotor technology–SMART," *Journal of Intelligent Material Systems and Structures*, vol. 15, no. 4, pp. 249–260, 2004.

[14] L. R. Centolanza, E. C. Smith, and B. Munsky, "Induced-shear piezoelectric actuators for rotor blade trailing edge flaps," *Smart Materials and Structures*, vol. 11, no. 1, pp. 24–35, 2002.

[15] B. Woods, E. Bubert, C. Kothera, J. Sirohi, and N. Wereley, "Experimental testing of pneumatic artificial muscles for trailing edge flap actuation," in *48th AIAA/ASME/ASCE/AHS/ASC Structures, Structural Dynamics, and Materials Conference*, Honolulu, Hawaii, USA, 2007.

[16] R. Jain, K.-Y. Szema, R. Munipalli, H. Yeo, and I. Chopra, "CFD-CSD analysis of active control of helicopter rotor for performance improvement," in *The American Helicopter Society 65th Annual Forum*, pp. 2467–2486, Grapevine, Texas, USA, 2009.

[17] A. Gagliardi and G. N. Barakos, "Analysis and design of a flap-equipped low-twist rotor for hover," *Journal of Aircraft*, vol. 46, no. 1, pp. 74–84, 2009.

[18] A. Jose and J. Baeder, "Steady and unsteady aerodynamic modeling of trailing edge flaps with overhang and gap using CFD and lower order models," in *47th AIAA Aerospace Sciences Meeting Including the New Horizons Forum and Aerospace Exposition*, p. 1071, Orlando, Florida, USA, 2009.

[19] J. F. Tan, Y. M. Sun, H. W. Wang, and C. L. Lin, "New approach for aerodynamic and aeroacoustic analysis of actively controlled flaps rotor," *Journal of Aircraft*, vol. 55, no. 6, pp. 2191–2202, 2018.

[20] A. A. Hassan, F. K. Straub, and K. W. Noonan, "Experimental/numerical evaluation of integral trailing edge flaps for helicopter rotor applications," *Journal of the American Helicopter Society*, vol. 50, no. 1, pp. 3–17, 2005.

[21] S. Xing, H. Xu, W. Zhang, and G. Delibra, "Trailing edge flap effects on dynamic stall vortex and unsteady aerodynamic forces on a pitching airfoil," *International Journal of Aerospace Engineering*, vol. 2022, Article ID 1674074, 20 pages, 2022.

[22] F. Kody, M. D. Maughmer, and S. Schmitz, "Non-harmonic deployment of active devices for rotor performance enhancement," in *The American Helicopter Society 69th Annual Forum*, pp. 2215–2227, Phoenix, Arizona, USA, 2013.

[23] F. Kody, E. Corle, M. D. Maughmer, and S. Schmitz, "Higher-harmonic deployment of trailing-edge flaps for rotor-performance enhancement and vibration reduction," *Journal of Aircraft*, vol. 53, no. 2, pp. 333–342, 2016.

[24] Z. Hu, G. Xu, and Y. Shi, "A new study on the gap effect of an airfoil with active flap control based on the overset grid method," *International Journal of Aeronautical and Space Sciences*, vol. 22, no. 4, pp. 779–801, 2021.

[25] R. Jain, H. Yeo, and I. Chopra, "Investigation of trailing-edge flap gap effects on rotor performance using high-fidelity analysis," *Journal of Aircraft*, vol. 50, no. 1, pp. 140–151, 2013.

[26] N. Liggett and M. J. Smith, "The physics of modeling unsteady flaps with gaps," *Journal of Fluids and Structures*, vol. 38, pp. 255–272, 2013.

[27] Z. Hu, G. Xu, and Y. Shi, "A robust overset assembly method for multiple overlapping bodies," *International Journal for Numerical Methods in Fluids*, vol. 93, no. 3, pp. 653–682, 2021.

[28] Z. Hu, Y. Shi, Y. Yang, and G. Xu, "A modeling method and system for complex motion description. China Invention patent ZL201910187086.6, filed November 20th," 2020.

[29] Z. Hu, G. Xu, Y. Shi, and R. Xia, "Airfoil–vortex interaction noise control mechanism based on active flap control," *Journal of Aerospace Engineering*, vol. 35, no. 1, article 4021111, 2022.

[30] R. C. Strawn, E. P. N. Durlue, and J. Ahmatl, "Rotorcraft aeroacoustics computations with overset-grid CFD methods," *Journal of the American Helicopter Society*, vol. 44, no. 2, pp. 132–140, 1999.

[31] J. L. Cross and W. Tu, "Tabulation of data from the tip aerodynamics and acoustics test," NASA-TM-102280, 1990.

[32] F. Farassat, "Derivation of formulations 1 and 1A of Farassat," NASA/TM-2007-214853, 2007.

[33] J. G. Leishman, *Principles of Helicopter Aerodynamics*, Cambridge University Press, New York, NY, USA, 2006.

[34] C. Bak, M. Gaunaa, P. B. Andersen, T. Buhl, P. Hansen, and K. Clemmensen, "Wind tunnel test on airfoil Risø-B1-18 with an active trailing edge flap," *Wind Energy*, vol. 13, no. 2-3, pp. 207–219, 2010.